Pontifícia Universidade Católica
do Rio de Janeiro

Rodrigo Gomes Costa

Ion Treatments on Two-dimensional Molybdenum Disulfide

Tese de Doutorado

Thesis presented to the Programa de Pós-graduação em Física of PUC-Rio in partial fulfillment of the requirements for the degree of Doutor em Ciências - Física

Advisor: Prof. Marcelo Eduardo Huguenin Maia da Costa

Rio de Janeiro
April 2024

Pontifícia Universidade Católica
do Rio de Janeiro

Rodrigo Gomes Costa

Ion Treatments on Two-dimensional Molybdenum Disulfide

Thesis presented to the Programa de Pós-graduação em Física of PUC-Rio in partial fulfillment of the requirements for the degree of Doutor em Ciências - Física. Approved by the Examination Committee:

Prof. Marcelo Eduardo Huguenin Maia da Costa
Advisor
Departamento de Física – PUC-Rio

Dr. Neileth Johanna Stand Figueroa
Departamento de Física – PUC-Rio

Prof. Victor Carôzo Gois de Oliveira
Departamento de Física – PUC-Rio

Prof. Luiz Fernando Zagonel
UNICAMP

Prof. Cláudio Radtke
UFRGS

Rio de Janeiro, April 5th, 2024

Rodrigo Gomes Costa

Bachelor and Master in Physics by the Universidade Federal de Juiz de Fora.

Bibliographic data

Costa, R.G.

Ion Treatments on Two-dimensional Molybdenum Disulfide / Rodrigo Gomes Costa; advisor: Marcelo Eduardo Huguenin Maia da Costa. – 2024.

80 f: il. color. ; 30 cm

Tese (doutorado) - Pontifícia Universidade Católica do Rio de Janeiro, Departamento de Física, 2024.

Inclui bibliografia

1. Física – Teses. 2. materiais bidimensionais. 3. tratamento com íons. 4. espectroscopia Raman. 5. fotoluminescência. 6. dissulteto de molibdênio. I. Costa, M.. II. Pontifícia Universidade Católica do Rio de Janeiro. Departamento de Física. III. Título.

CDD: 004

Dedicated to all the people who lost their lives during the COVID-19 pandemic.

Acknowledgments

To my parents and brother, who never ceased to believe in my path.

To my advisor Professor Marcelo for the stimulus and partnership to carry out this work, the precious discussions, and above all, the patience.

To Dr. André Barbosa for having the most kind spirit and good-faith to teach me so much without asking anything in return.

To my colleagues and Professors from VDG and the Physics Department, for being so helpful all the time.

To my friends, close and far away, who made my life sweeter during the bitter times of the pandemic.

To Morgana, Madruga, Mel, Luna, Catarina, Aurora, Fred, and Toddy (in memoriam).

To CAPES, CNPq, and PUC-Rio, for the aids granted, without which this work does not could have been accomplished.

This study was financed in part by the Coordenação de Aperfeiçoamento de Pessoal de Nível Superior - Brasil (CAPES) - Finance Code 001.

Last, but not least, to Yohanna Guimarães, whose love held-me tenderly though the difficulties and for keeping the flame of knowledge alive in me. I love you.

Abstract

Costa, R.G.; Costa, M. (Advisor). **Ion Treatments on Two-dimensional Molybdenum Disulfide**. Rio de Janeiro, 2024. 80p. Tese de Doutorado – Departamento de Física, Pontifícia Universidade Católica do Rio de Janeiro.

Two-dimensional molybdenum disulfide (2D MoS_2) has gained significant attention due to its unique electronic and optical properties, making it a promising material for various applications, such as optoelectronic devices and energy storage systems. This thesis investigates methods to enhance the photoluminescence (PL) emission of monolayer MoS_2 through different treatments. The experiments performed aimed to achieve this by creating defects on the crystal structure in a controlled manner, attacking the 2D MoS_2 with ions. The samples were obtained via Chemical Vapor Deposition (CVD). The changes in morphology and electro-optical features were assessed via Atomic Force Microscopy (AFM), Resonant Raman Spectroscopy, and Photoluminescence (PL) Spectroscopy.

The first round of experiments employed a Nitrogen Plasma treatment. AFM evidence of the integrity of the morphology is presented, although the PL signal was significantly quenched for the parameters used. Raman Spectroscopy shows an evolution of key features as defects are progressively created, namely the second-order 2LA(K) and 2LA(M) vibrational modes Full Width at Half Maximum (FWHM).

Afterwards, a Helium ion beam treatment was applied, yielding positive results when controlling treatment time and energy. Photoluminescence emission spectra revealed the signal intensity was enhanced by up to a factor of 2. Resonant Raman measurements indicated a controlled defect creation was achieved (with practically unchanged second-order features). AFM analysis demonstrated no change in the micrometer scale dut to the treatments. This treatment constitutes a facile method for enhancing CVD grown monolayer MoS_2 samples PL emission for future device applications.

Keywords

Two-dimensional materials; Ion treatment; Raman Spectroscopy; photoluminescence; Molybdenum Disulfide.

Resumo

Costa, R.G.; Costa, M.. **Tratamentos com íons sobre dissulfeto de molibdênio bidimensional**. Rio de Janeiro, 2024. 80p. PhD Thesis – Departamento de Física, Pontifícia Universidade Católica do Rio de Janeiro.

O dissulfeto de molibdênio bidimensional (MoS_2 2D) tem atraído significativa atenção devido às suas propriedades eletrônicas e ópticas únicas, tornando-se um material promissor para diversas aplicações, como dispositivos optoeletrônicos e sistemas de armazenamento de energia. Esta tese investiga métodos para aprimorar a emissão de fotoluminescência (PL) de MoS_2 monocamada por meio de diferentes tratamentos. Os experimentos realizados visaram criar defeitos na estrutura cristalina de forma controlada, atacando o MoS_2 2D com íons. As amostras foram obtidas via Deposição Química a Vapor (CVD). As alterações morfológicas e características eletro-ópticas foram avaliadas por Microscopia de Força Atômica (AFM), Espectroscopia Raman Ressonante e Espectroscopia de Fotoluminescência (PL).

A primeira rodada de experimentos utilizou um tratamento de Plasma de Nitrogênio. Evidências de AFM da integridade da morfologia são apresentadas, embora o sinal de PL tenha sido significativamente atenuado para os parâmetros utilizados. A Espectroscopia Raman mostra uma evolução de características-chave à medida que defeitos são progressivamente criados, a saber, a Largura a Meia Altura (FWHM) dos modos vibracionais de segunda ordem 2LA(K) e 2LA(M).

Posteriormente, um tratamento com feixes de íons de Hélio foi aplicado, levando a resultados positivos ao controlar o tempo e a energia do tratamento. Os espectros de emissão de fotoluminescência revelam que a intensidade do sinal foi aumentada em até duas vezes. Medidas de Raman Ressonante indicaram que a criação de defeitos foi controlada (com características de segunda ordem praticamente inalteradas). A análise de AFM demonstrou que não houve mudança da escala micrométrica devido aos tratamentos. Este tratamento constitui um método fácil para aprimorar a emissão de fotoluminescência de amostras de MoS_2 monocamada crescidas via CVD para futuras aplicações em dispositivos.

Palavras-chave

materiais bidimensionais; tratamento com íons; espectroscopia Raman; fotoluminescência; dissulteto de molibdênio.

Table of contents

List of figures

List of tables

List of Abreviations

2D – Two-dimensional

TMD – Transition-Metal Dichalcogenide

MoS_2 – Molybdenum Disulfide

PL – Photoluminescence

CVD – Chemical Vapor Deposition

MOCVD - Metal Organic Chemical Vapor Deposition

MFC – Mass Flow Controller

PLC – Programmable Logic Controller

AFM – Atomic Force Microscopy

SPM – Scanning Probe Microscopy

FWHM – Full Width at Half Maximum

eV – Electron-Volt

DFT – Density Functional Theory

HER – Hydrogen Evolution Reaction

RF – Radio Frequency

EBL – Electron-beam Lithography

FET – Field-effect Transistor

STEM – Scanning Transmission Electron Microscopy

I shall be telling this with a sigh
Somewhere ages and ages hence:
Two roads diverged in a wood, and I—
I took the one less traveled by,
And that has made all the difference.

Robert Frost, *The Road Not Taken.*

1
Introduction

The scientific community became interested in researching two-dimensional systems since the realization of Graphene by Andre Geim and Konstantin Novoselov in 2004 [1]. Graphene is ideally a zero-gap semiconductor [2]. Due to its crystal structure graphene has an interesting band structure, giving its charge carriers a relativistic behavior near its K and K' points in Brillouin Zone ($1/300^{th}$ the speed of light in vacuum), with mobilities as high as 16000 $cm^2V^{-1}s^{-1}$ [3]. It is very mechanically resistant, with a tensile fracturing strength around 50 GPa [4]. It absorbs all visible light wavelengths and yet is transparent due to its thickness [5]. Although Graphene has interesting properties, its lack of natural band-gap lead to the search of 2D materials in which it occurs naturally as means to facilitate their usage in nano electronics applications.

An alternative is two-dimensional Transition metal dichalcogenides (2D TMDs)[6]. They are a set of layered materials interconnected via Van der Waals forces. In their intrinsic (i.e. non-doped) form their unit cell is composed of a transition metal atom M (e.g. Mo, W) and two chalcogen atoms X (e.g. S, Se, Te) under the chemical formula MX_2 [7]. Different representatives of these materials present different properties, some are semiconducting with a direct bandgap, some are semimetallic [8]. Hence, 2D TMDs account for a promising platform for future nanostructured devices, such as: photodetectors [9, 10, 11], transistors [12], p-n junctions [13, 14, 15], photovoltaic cells [16], and as catalysts in hydrogen evolution reaction (HER) [17, 18].

Hence an interesting question is how to modify or tune the TMDs optoelectronical, thermal, and mechanical properties to extend their range of applications. Regarding the optoelectronical properties, many approaches were taken in order to enhance 2D TMDs photoluminescence, modify their bandgap, passivate the surface or induce some property of interest (e.g., doping, chemical treatments, surface modification, defect engineering)[19, 20, 21, 22, 23].

This thesis is focused in performing low-energy ion treatments aiming to improve two-dimensional monolayer Molybdenum Disulfide (MoS_2) Photoluminescence emission. This is of particular interest to applications such as optoelectronic devices, gas sensors, and photodetectors.

1.1 Outline

Though the reader might be acquainted with the concepts needed to comprehend the experiments in totality, the document was written to be as linear as possible for ease of navigation through the text.

The text is divided in seven chapters: after this Introduction some theoretical aspects will be covered in Chapter 2. Subsequently in Chapter 3 some relevant literature that forms a background to this thesis will be discussed, followed by the thesis proposal in Chapter 4. Then Chapters 5 and 6 are dedicated to show the experiments performed, their employed methodologies, highlighting the key differences between them and the obtained results. Finally, Chapter 7 offers the conclusions.

2
Theoretical Aspects

In this chapter basic theoretical aspects to the comprehension of the experiments performed and the results obtained are introduced.

2.1
Chemical Vapor Deposition

There is a handful of methods used to synthesize two-dimensional materials. They are categorized in two different approaches: (i) top-down, where one reduces dimensionality from bulk material (e.g. mechanical exfoliation); and (ii) bottom-up, where the 2D material is built from scratch. Chemical Vapor Deposition (CVD) is a bottom-up type growth technique that has been favored in industrial processes for its relative low cost (e.g., compared to Molecular Beam Epitaxy) and scalability. It is also used extensively in research environments due to its relative ease of implementation and trouble-shooting.

In general, CVD synthesis is based on the chemical combination of precursors in their gaseous phases on a substrate [24]. Figure 2.1 provides a simple visual depiction of a generic CVD process inside a horizontal tube: (a) the reactant gases are transported into the tube; (b) the gases directly diffuse through the boundary layer; (c) the chemical species adsorb onto the substrate; alternatively the gas species could react (d) before reaching the substrate; (e) the adsorbed species undergo surface diffusion and reactions take place on the surface of substrate and to form the desired structure; (f) some by-products and unreacted species might be desorbed from the surface and escape the tube. This description is generic in the sense that the each chemical reaction will take place in a certain kinetic and thermodynamical state that might modify what is possible or not to happen. Usually some form of energy must be dispensed for the chemical reactions to occur, the most common way to perform this is by rising the temperature of the system. There are numerous factors to account for when performing a CVD experiment that are not always clear, or cannot be easily controlled, such as variations in geometry, the atmospheric pressure, air moisture, how clean the reactor and substrate-holder can be, etc.

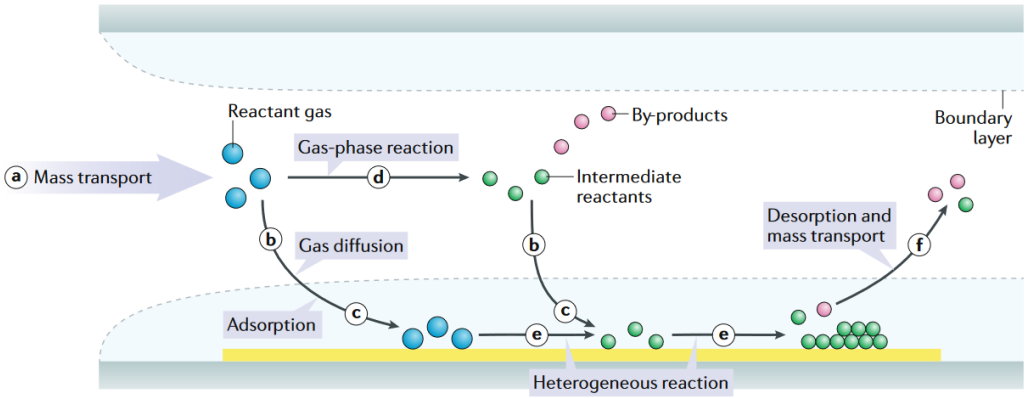

Figure 2.1: A step-by-step generic CVD reaction schematics. Adapted from [25].

Regarding instrumentation, Sun *et al.* categorize the CVD experiment requirements in [25]: a carrying mechanism to the gas phase reactants; an isolated environment to carry out the reactions (i.e. a reaction chamber); evacuation of gases and reaction pressure control; an energy supply to the chemical reactions; an exhaust system for the gases, and an automatic process control. Different gases are used as carrier species–which deliver the chemical precursors to the substrates–the carrier gas itself can be a reactant or an inert gas. The gas lines are typically fed from canisters connected to Mass Flow Controllers that can set the gas flow rate. The reaction chamber can take many geometries, the most usual are a cylindrical shaped quartz tube or metallic alloy chamber. The reaction chamber is connected to the carrier gas line and can be positioned horizontally or vertically in relation to the gas flow. The substrate placed inside the chamber is usually supported onto a substrate holder (e.g., a crucible), which can be made of quartz, alumina, graphite, or other materials. At the downstream end of the reaction chamber a vacuum pump can be connected if a pressure lower than the atmospheric is desired, which will need to be monitored during the experiment. The fumes released must be filtered and collected to an external environment for safety measures, and if any toxic by products are expelled an additional trapping system should be implemented (e.g. a water-based particle trap). The energy source for the chemical reactions is usually an electric resistance connected to a current source that heats the substrate region. In some experiments an electrical current is set inside the reaction chamber creating a gas plasma as another energy source. The most common temperature sensor used in this type of setup is a thermocouple. To drive the whole CVD system to the growth state described some kind of automation is needed for the gaseous species flow and energy rise rate, this usually comes with Mass Flow Controllers (MFCs)

and Programmable Logic Controllers (PLCs). After growth, the system can be cooled naturally or assisted artificially, whether a type should be favored instead of another depends on experiment-dependent factors such as a possible mismatch between the thermal expansion coefficients of the desired structure and the substrate employed. It is important to notice the substrate choice is also relevant, it might act as an inert surface or as a catalyst, and its properties will affect subsequent measurements, in some cases the substrate needs to be removed completely after growth.

2.2 Optical Processes

A range of phenomena can occur when a material is subjected to light. This depends on the energy of incident photons and the possible optical transitions of the media [26]. These processes encompass light absorption, scattering, transmittance, and reflection. Of particular interest are two possibilities: (i) inelastic scattering of light by phonons, known as Raman Scattering, and (ii) the emission of light at a specific wavelength subsequent to absorption, called Photoluminescence.

2.2.1 Raman Scattering

When a material medium scatters light via optical phonons there are two possibilities: an elastic scattering where the incident photon field frequency is preserved (known as Rayleigh Scattering), and an inelastic scattering where the frequency is altered. The frequency change is due to the transfer of energy to the vibrational modes of the medium. This phenomenon was first reported by Sir C. V. Raman and K. S. Krishnan in 1928 [27], for which the former was awarded the Nobel Prize in Physics in 1930.

It is possible to understand this phenomenon with classical electromagnetism. An electric field $\mathbf{E}$ applied to a medium yields

$$\mathbf{P} = \alpha \cdot \mathbf{E}$$

where α is the polarizability tensor of the atom in the solid [26]. Lattice vibrations in a solid with a certain frequency ω_q modulate the polarizability[1] of the atoms which become

[1] An example is the stretching vibration mode of the linear carbon dioxide molecule (O=C=O). The polarizability is higher when the oxygen atoms are farther away from the molecule's center of mass.

$$\alpha = \alpha_0 \ + \ \alpha_1 \ sin \ \omega_i t$$

Assuming a monochromatic light source oscillating with frequency ω_i, that is

$$\mathbf{E} = \mathbf{E_0} \ sin \ \omega_i t$$

the polarization induced by such electric field will be

$$\begin{aligned} \mathbf{P} &= \mathbf{E_0}(\alpha_0 \ + \ \alpha_1 \ sin \ \omega_i t) sin \ \omega_i t \\ &= \mathbf{E_0} \left[\alpha_0 \ sin \ \omega_i t \ + \frac{1}{2} \alpha_1 \ cos(\omega_i - \omega_q)t - \frac{1}{2} \alpha_1 \ cos(\omega_i + \omega_q)t \right]. \end{aligned}$$

These terms mean the incident light will be scattered (i) elastically with the same frequency ω_i, and (ii) inelastically with altered frequencies, namely a downshift and a upshift by the frequency ω_q. The scattered light is collected and the Raman plot is created showing the scattered photons intensity vs the difference in energy of the incident photons and the scattered ones[2]. The most common form of measurement looks to scattered photons which suffered a downshift in frequency (i.e. Stokes process), these are generally more intense due to phonon creation and annihilation statistics. Since the elastic contribution is orders of magnitude higher it has to be mitigated with filters and/or via software. These phenomena are portrayed in figure 2.2.

[2]This energy difference is called Raman Shift or Wavenumber, usually expressed in units of cm^{-1}. The definition of Wavenumber used here is $k = 1/\lambda$.

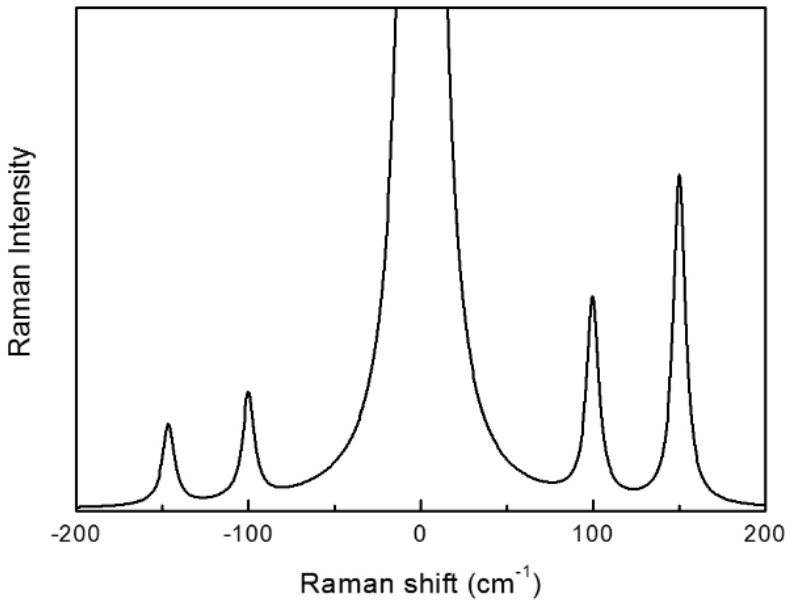

Figure 2.2: Generic Raman spectrum showing the Rayleigh scattering at the center (0 cm^{-1}), the Stokes process in the positive frequency axis, and the anti-Stokes process in the negative part. Adapted from [26].

The intensity of Raman scattering in quantum description is an application of the Fermi Golden Rule, which relates the transition rate between initial and final states to the the perturbation Hamiltonian. In the context of Raman scattering, a first order[3] process with excitation source of energy E_L can be expressed as [28]:

$$I(\omega_q, E_L) = \left| \sum_{\mathrm{i,m,m'}} \frac{\langle f|\nabla|m'\rangle\langle m'|H_{el-ph}|m\rangle\langle m|\nabla|i\rangle}{(E_L - \Delta E_{mi})(E_L - \hbar\omega_q - \Delta E_{m'i})} \right|^2$$

where $\Delta E_{mi} = (E_m - E_i) - i\gamma_r$, and i, m, m', and f are the initial, two intermediate and final states; γ_r is a spectral width due to the uncertainty principle. The $\langle m|\nabla|i\rangle$ and $\langle f|\nabla|m'\rangle$ terms are the electron-photon interaction of the optical absorption, and $\langle m'|H_{el-ph}|m\rangle$ is the matrix element for the electron-phonon interaction. Considering a Stokes process, where a phonon is created, we can divide the Raman scattering phenomenon in three parts: (i) the photon is absorbed and promotes an electron to an excited state m; (ii) the electron-phonon interaction takes place, leading the electron to a new state m' while creating a phonon with momentum $\hbar\omega_q$; (iii) the electron in the state m' is decays to an state f, releasing a photon with corresponding energy that will be measured.

[3]Order in this context means the number of scattering events. First order Stokes (anti-Stokes) scattering creates (annihilates) one phonon in the crystal.

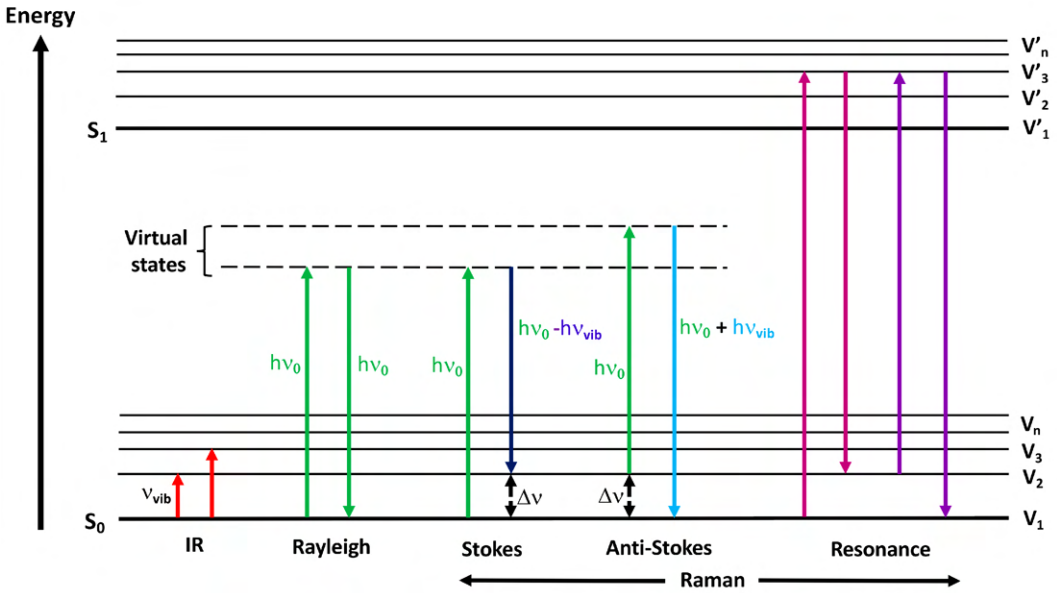

Figure 2.3: Jablonski diagram showing the transitions involved during infrared (IR) absorption, Rayleigh scattering, Stokes and anti-Stokes Raman Scattering, and Resonance Raman scattering. Adapted from [29].

The intermediate states m, m' are not necessarily real possible electronic states, they are called virtual states. If the incoming radiation of energy E_L is close to the material bandgap energy, the probability of a Raman scattering transition is significantly amplified; equally if the scattered light is close to the bandgap. This is called Resonance Raman scattering, where the intensity of observed peaks are orders of magnitude higher in comparison with non-resonant excitation energies. A Jablonski diagram illustrating these possible transitions is exhibited in figure 2.3.

2.2.2 Photoluminescence

Photoluminescence[4] (PL) refers to the spontaneous emission of light from a material after optical excitation, and Photoluminescence Spectroscopy refers to the analysis of this optical activity [31]. Figure 2.4 illustrates the photoluminescence process: when a semiconductor is subjected to a photon field with an energy larger than its band-gap, the energy of a photon can be absorbed[5] to promote an electron from the valence band to the conduction band (represented by the levels S_0 and S_1); In the conduction band, the photoexcited charge carrier can go though a vibrational relaxation (thus

[4]In Chemistry and Biology contexts Photoluminescence is often referred to as Fluorescence [30].

[5]This absorption means the whole photoluminescence process is subjected to electrical dipole selection rules.

generating heat) to the bottom of the conduction band, where finally it decays to its initial state radiatively, emitting a photon with energy correnponding to the bandgap $h\nu = E_g$. Another possibility is before the radiative emission an intersystem crossing happens, where the the charge carrier changes its spin state (e.g. going from a singlet state to a triplet state); this originates the so-called phosphorescence, a process characterized by being a slower form of luminescence. An important aspect is the radiative decay is much more probable when the semiconductor has a direct bandgap, meaning the charge carrier will not need to change its momentum before being converted to a photon, since the top of the valence band and the bottom of the conduction band both lie in the same point of the Brillouin zone.

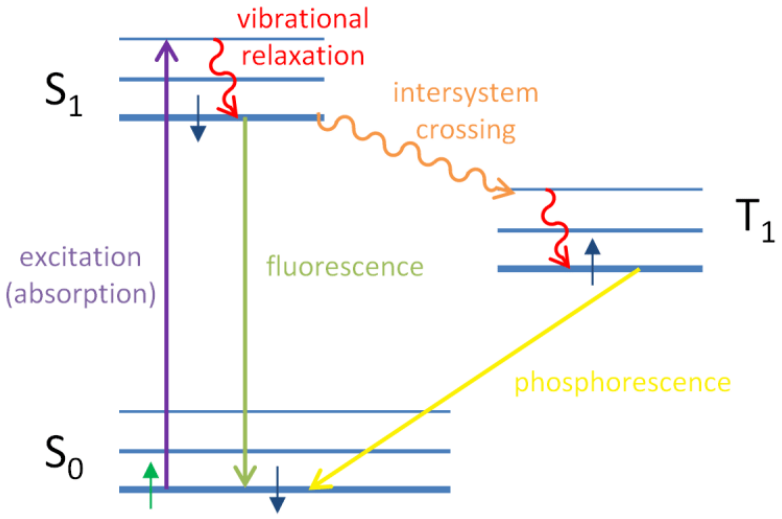

Figure 2.4: Illustration of the steps of a luminescence emission process. Adapted from [32].

2.3 Atomic Force Microscopy

Introduced in 1986 by Binnig *et al.* [33] as a category of Scanning Probe Microscopy (SPM), Atomic Force Microscopy (AFM) is a technique employed for visualizing surface topography. An image is achieved scanning the sample with a tip on a cantilever, and recording the information of this interaction (namely, the force) while they move in relation to each other. Diverse types of instrumentation, probes, modes of measurement, and strategies for data collection exist, each one with its particular strengths and limitations.

The probe tip is usually made of Silicon or Silicon Nitride, with the smallest tip radius possible for increased resolution (typical dimensions are a tip radius in the order of nanometers and tip height in the order of micrometers). The tip is part of a cantilever, and it is also used to detected

the signal which is transduced to topography and force information. This is done recording the deflection of the cantilever, and can be done via laser deflection on the top of the cantilever, interferometry, change of capacitance, of piezoresistance, or piezoelectricity [34]. Figure 2.5 shows a scheme of the most commonly used form of deflection, where a laser beam reaches the cantilever's top surface and is reflected onto a four-segment photodiode. The vertical displacement represents the normal bending and the lateral displacement represents the torsion which the cantilever is subjected to. Scanning the sample and record its topography requires the ability to move it (or the sensors), the most used system is a piezoelectric stage (the cylindrical object displayed on figure 2.5), which is used to support the sample of interest. The data recording is managed via specialized computer software. And the treated data showing topography is usually presented in a pseudo-color palette.

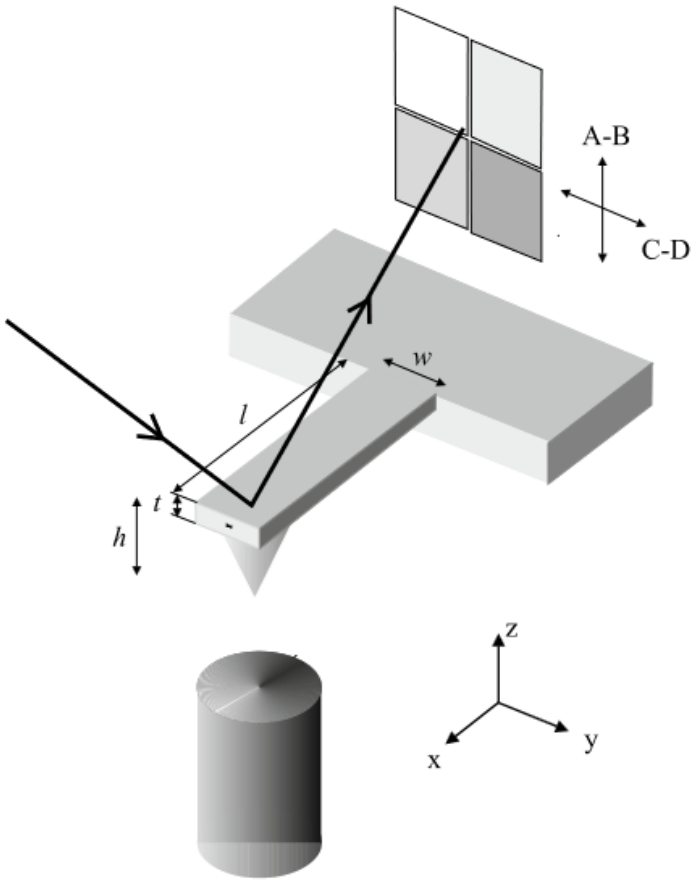

Figure 2.5: Diagram of the cantilever deflection sensoring. A laser beam is reflected onto a four-segment photodiode. The A-B signal is proportional to the normal force and the C-D signal is proportional to the lateral force. Adapted from [34].

Different measurement modes are implemented in AFM systems for different purposes and sample characteristics. The most common modes for

constructing a topographic image are: contact mode, non-contact mode, and semi-contact mode. In contact mode, the AFM tip is in constant contact with the sample surface while scanning. The tip interacts with the surface, causing a deflection in the cantilever, which is detected and used to generate an image of the surface topography. Inversely, the AFM tip in non-contact mode does not touch the sample surface during scanning, it oscillates near the surface at a certain distance. Observed changes in the oscillation amplitude or frequency due to interactions with the surface are used to create an image. Finally, in semi-contact mode (also known as tapping mode), the AFM tip taps the sample surface intermittently while scanning. This tapping minimizes lateral forces and reduces damage to both the tip and the sample compared to continuous contact mode.

2.4 2D Transition-Metal Dichalcogenides

Two-dimensional Transition-Metal Dichalcogenides (2D TMDs) constitute a set of layered compounds with distinct and interesting properties. A monolayer is composed of a transition metal atom layer M (e.g., Mo, W, Re, Nb, V) "sandwiched" between two calchogenide atom layers X (e.g., S, Se, Te), with chemical formula MX_2. Incidentally, the so-called monolayer is in reality composed of three atomic layers (contrasting with one for single-layer Graphene, for instance). Multilayer and bulk TMDs are formed by stacking monolayers, they are connected by weak Van der Waals interaction, making them relatively easy to exfoliate (while the in-plane chemical bonds are covalent-ionic). Different TMDs present different electronic properties; they can be semiconducting, metallic, and even superconducting [35]. Figure 2.6 shows the crystal structures of a generic monolayer TMD in the phases 2H, 1T, and 1T'. These phases represent the relative position of the atoms in the lattice and can influence the electric properties of a given TMD [36].

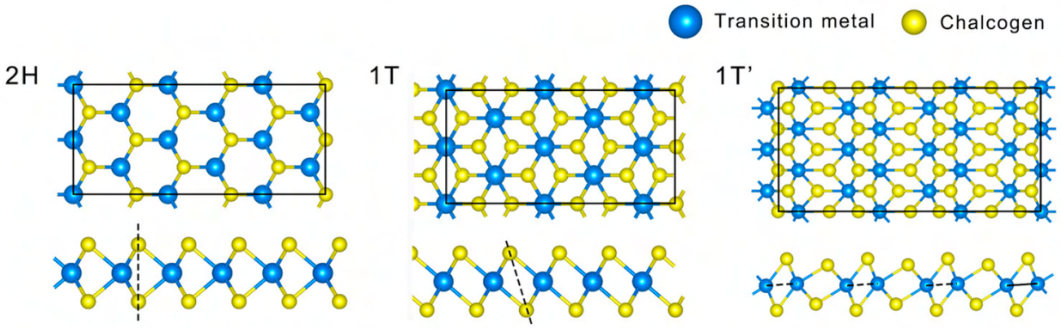

Figure 2.6: Top and lateral view of monolayer TMD crystal structures in 2H, 1T, and 1T' phases. Adapted from [36].

2.4.1 Two-dimensional Molybdenum Disulfide

Molybdenum Disulfide (MoS_2) already had an application as a dry lubricant before being isolated in its two-dimensional form. Novoselov *et al.* were the first to report on two-dimensional MoS_2 crystals obtained via micromechanical cleavage, among other 2D crystals [37]. As graphene in comparison to graphite, TMDs in general exhibit characteristics in mono or few-layer form different from their bulk counterparts. MoS_2, goes through an indirect-to-direct band-gap transition as one goes from bulk to monolayer [38], as depicted in figure 2.7. Decreasing the thickness changes the band structure near the Γ point, while the region around the K point remains practically unchanged. Bulk and monolayer 2H-MoS_2 are semiconductors with calculated bandgap values of 0.88 and 1.71 eV, respectively. Experimental values are reported in different values up to 2.16 eV in monolayers [39]. Because of this interesting characteristic, MoS_2 photoluminescence increases when one goes from bulk to monolayer, as described in section 2.2.2.

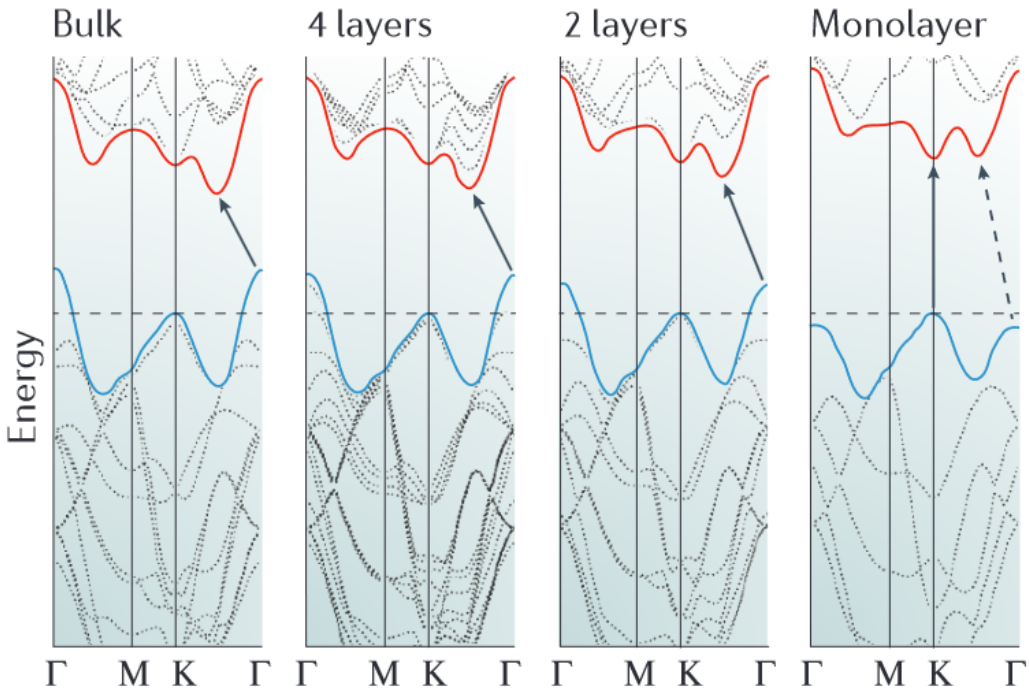

Figure 2.7: Band structure of 2H-MoS_2 calculated for samples of decreasing thickness. It is possible to see the bandgap increases and becomes direct as the number of layers is reduced to one. Adapted from [7].

This indirect-to-direct bandgap transition results in an improved photoluminescence emission, since the photoexcited charge carriers do not need to change their momentum prior to radiative decay, making the photoluminescent emission orders of magnitude more intense in direct bandgap semiconductors.

This is observed in 2D MoS_2, as shown in figure 2.8, where the PL emission rises as the number of layers decreases. Another important feature shown in figure 2.8 is the non-resonant Raman spectra of 2D MoS_2, which present two characteristic peaks: the in-plane vibrational mode E^1_{2g} and the out-of-plane vibrational mode A_{1g}[6]. These spectral features act as a fingerprint to assess the existence of MoS_2 in a given sample, and their change upon any sample modification can give information about induced strain, doping, and loss of crystallinity.

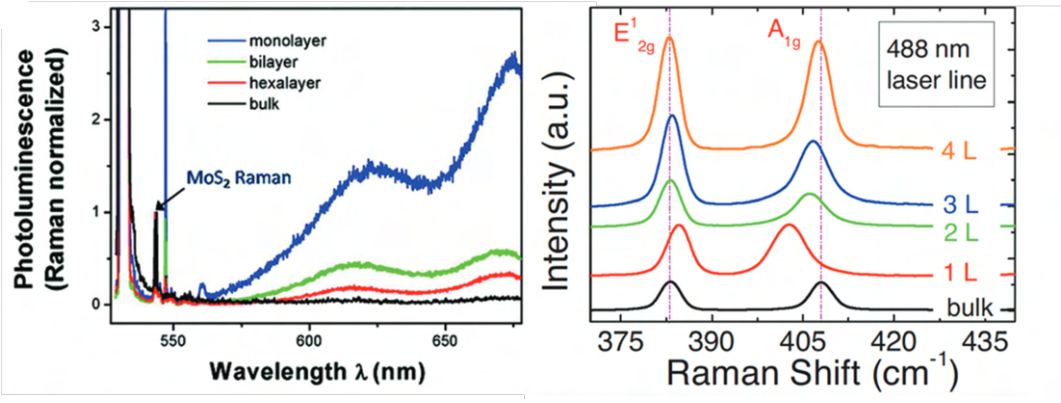

Figure 2.8: Normalized (to the Si Raman peak) Photoluminescence emission and Raman spectra of MoS_2 with different amount of layers. One can observe the emission rises as the number of layers decrease; and the distance between the vibrational modes E^1_{2g} and A_{1g} decrease down to around 20 cm^{-1} as the number of layers decrease. Adapted from [38] and [40].

Regarding the lineshape of PL emission in monolayered MoS_2, there are three largely observed contributtions. Its band structure have two direct-gap non-equivalent valleys with identical bands but with opposite spins due to time-reversal symmetry [41]. This separation give rise to two possible radiative emissions with slightly different energies, called excitons A and B, as illustrated in the inset of figure 2.9. The reduced dimensionality of MoS_2 reduces dielectric screening, thus forming strong interactions and many-body states such as trions. A trion is a three body structure formed when either an electron or hole binds to an exciton [42]. A negative trion is often observed in MoS_2 due to its natural n-doping, with an energy less than the exciton A. Figure 2.9 shows a deconvolution of a monolayer MoS_2 PL spectrum highlighting these different contributtions.

[6]According to Group Theory, the correct modes nomenclature for monolayers is E' and A'$_1$, while E^1_{2g} and A_{1g} are for bulk. It is common to find the bulk nomenclature being used for monolayers in literature [40].

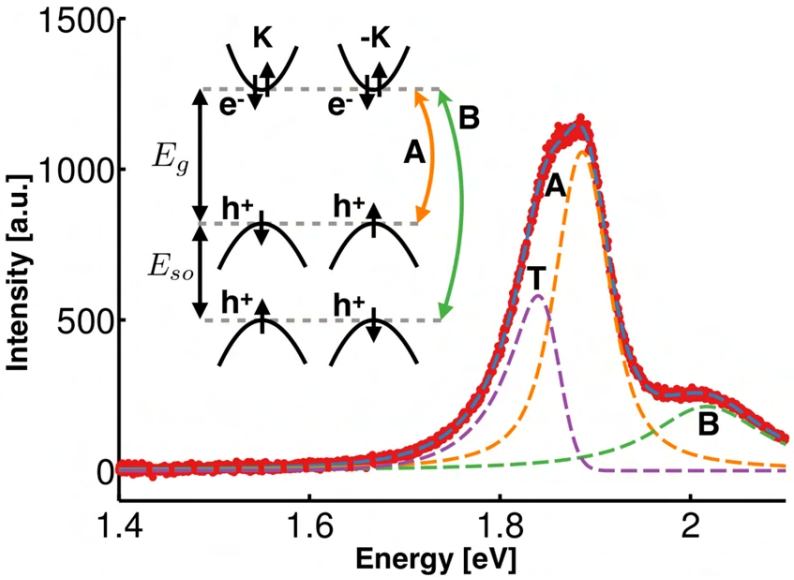

Figure 2.9: Deconvoluted PL spectrum of monolayer MoS_2 at 273 K. A and B denote excitons, and T denotes the trion. Inset: Band structure near the K and $-K$ points of the Brillouin zone with band gap, E_g around 1.9 eV, and spin-orbit splitting, E_{so} around 140 meV. Adapted from [42].

3
State of the Art

In this chapter, relevant literature is discussed on different approaches to modify properties of 2D MoS_2. In particular treatments that consist of modifying the 2D structures with ionized gas species are considered. Previous studies demonstrated that TMDs respond differently to treatments applied, this response depends on both the TMDs and treatment conditions, mainly the energy and gas species.

Kang *et al.* modified exfoliated MoS_2 monolayer samples via an Oxygen Plasma treatment [43]. The researchers used a Plasma Etching system operating at 100 W power at 50 kHz, using a mixture of Oxygen and Argon (1:4 ratio). The treatment times up to 6 seconds (in increments of 1 s) resulted in a quenched Photoluminescence signal. The presented results revealed that each passing second quenched more the PL signal until its extinction. X-Ray Photoelectron Spectroscopy (XPS) evidence suggested the Plasma was not only creating defects, but the presence of Oxygen was creating MoO_3, where they argued major lattice distortions were being induced by this process. The presented Raman (non-resonant) spectra shown the Full Width at Half Maxium (FWHM) of the vibrational modes A' and E' increased significantly (up to 5 and 15 cm^{-1}, respectively). They also verified a blueshift in the A' mode position and a redshift in the E' mode position. It is not mentioned in this work, but this is an evidence of strain and p-doping occurring in their samples. Finally this work presents very interesting Density Functional Theory (DFT) calculations of monolayer MoS_2 and defective MoS_2, either by Oxygen defects or MoO_3 defects. They showed in every case but the pristine the simulation pointed to a direct-to-indirect bandgap transition induced by this type of defects.

Likewise, Kim *et al.* also used Oxygen plasma for MoS_2 surface modification [44]. However, there are key differences in this work in comparison to Kang *et al.* The authors start the process with a multilayer sample and reduce it to monolayer form subjecting it to a Radio Frequency (RF) powered Plasma with 21 W power. Raman spectroscopy proved they did not form MoO_3 defects, demonstrating the lower power O_2 plasma did not form this compound. Their XPS data showed some etched Sulfur atoms were substituted for Oxygen atoms. This group applied a plasma treatment that enhanced the PL signal, but in the sense of reducing dimensionality, not augmenting this characteristic in a initial monolayer sample.

Nguyen *et al.* tried to engineer the monolayer MoS_2 surface for a better performance in Hydrogen Evolution Reaction (HER) applications [45]. Pristine MoS_2 with its edges and occasional Sulfur vacancies is a suitable (but not optimal) material for this application, as these features act as sites for Hydrogen production, and the researchers tried to increase the number of active sites by applying a Nitrogen plasma. The authors grew the samples via metal organic chemical vapor deposition (MOCVD) technique using gas precursors onto a SiO_2 substrate. The plasma treatment experiment was performed with a N_2 injecting needle with a 20 kV potential difference between the tip and the sample. They tried treatment times of 0, 10, 20, 30, 40, and 50 min. Figure 3.1 displays their optical characterizations, where they observed the broadening of the fingerprint vibrational modes E^1_{2g} and A_{1g}, demonstrating the sample underwent defect creation. It is also possible to see all the times tested resulted in a PL intensity quenching. These results are interesting and will appear in a similar form later in the text. Eventually they succeeded in improving the MoS_2 efficiency in HER by creating more active sites. Azcatl *et al.* [46] attempted to dope exfoliated multilayer MoS_2 with nitrogen through a remote N_2 plasma surface treatment. They applied N_2 plasma using a 13.56 MHz RF plasma at a power of 100 W, using N_2 as gas source flowing at 45 sccm, at a substrate temperature of 300 °C. The samples were subjected to treatment in different times up to 60 min. The authors present XPS evidence they achieved a covalent bonding Mo-N, with an atomic percentage (at%) of nitrogen in MoS_2 up to 9% for the maximum exposure time. Their Raman spectra show a strong blueshift in the A_{1g} mode and a separation of the mode E^1_{2g} into two modes called E^{+1}_{2g} and E^{-1}_{2g}. This mode separation indicates their samples endured a significant amount of strain [47], which is supported by the amount of cracks apparent in their samples AFM images. The authors do not present PL data, which is comprehensible since there is no relevant emission when the samples are not monolayer.

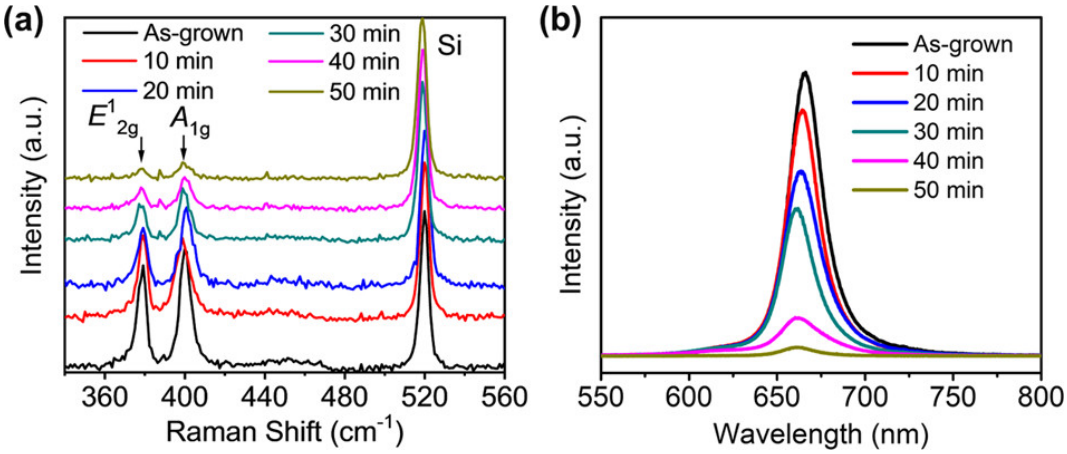

Figure 3.1: Evolution of Raman modes and PL characteristics of 1L-MoS_2 with Nitrogen plasma treatment. (a) Raman spectra shows the evolution of typical Raman modes, namely, E^1_{2g} and A_{1g} of MoS_2; (b) PL spectra as a function of treatment time. Adapted from [45].

Similarly, aiming improvement in HER applications of exfoliated monolayer MoS_2, Wang *et al.* used [48] both Argon and Oxygen plasma (in different experiments) in order to create more active sites. They used a fixed 50 W power and a gas flow of 100 sccm for both gas species, and a fixed treatment time. Unfortunately the article did not present PL data, but did show evidence of the same E^1_{2g} and A_{1g} peaks broadening observed by Nguyen *et al.*

In a different TMD, Tungsten Disulfide (WS_2), Barbosa *et al.* applied a low-power (7 W) Nitrogen plasma treatment with different times in order to modify the optical and electronic properties [49]. The samples were grown via CVD. The times used were 0, 1, 2, and 4 s. The shorter time of 1 second yielded a PL signal enhancement of 34 %; the vibrational characteristics are also presented, but are not directly comparable to MoS_2.

Jadwiszczak *et al.* aimed to increase the photoresponsivity[1] of monolayer MoS_2 by treatment with O_2:Ar (1:3) plasma [50]. Their samples were synthesized on SiO_2/Si substrates via CVD, and then a Field-effect Transistor (FET) was fabricated via Electron-beam Lithography (EBL). The plasma treatment was performed with a plasma cleaner for 2 s, utilizing O_2:Ar (1:3) gas mixture at a working pressure of 500 Pa. They presented a DC photoresponsivity plot showing the applied treatment indeed increased it for different transistor bias values. Raman spectra also observed E^1_{2g} and A_{1g} characteristic modes quenching and broadening, while PL spectra showed a correspondent signal quenching. Even with this PL signal quenching the authors managed to improve their device's performance, and they provided Scanning Electron

[1]In a photodetector device photoresponsivity is the electric current output per optical power input.

Microscopy (SEM) evidence the Oxygen treatment formed MoO_3 spanning all the surface. This work suggest the oxide formation along the surface creates a MoS_2/MoO_3 interface, and because they have different Fermi levels the subsequent band bending traps the photogenerated holes, thus quenching the PL signal, but contributing to the current output. This is an example where the device is improved even though the PL is reduced. In a similar device, but using multilayered MoS_2, the work of Li *et al.* [51] argued that deep trap[2] states can be filled when Oxygen ions are chemically bonded with MoS_2 at Sulfur Vacancy sites.

Huang *et al.* [52] argue that physical sputtering processes predominantly generate chalcogen defects, but highly energetic (or heavy) ions could displace Mo atoms. The authors proposed low-energy helium plasma treatment to achieve a selective sputtering of S atoms in monolayer MoS_2 without damaging the Mo sublattice. Apparently the group used commercially available CVD grown samples for XPS characterization, but the other techniques seem to have used exfoliated samples. They used a plasma gun at $1 \cdot 10^{-4}$ Torr, and the flux was $1.75 \cdot 10^{12}$ ions/cm^2/s. The times used were 10 minutes, 1 hour, and 2 hours. Presented XPS analysis demonstrated their approach indeed preserved the Mo layer while removing S atoms. This is also observed in the Scanning Transmission Electron Microscopy (STEM) image (figure 3.2), where monosulfur vacancies (VS) and disulfur vacancies (VS_2) are highlighted. Photoluminescence spectra presented revealed the emission intensity decreased as consequence of the treatment applied. Additionally, Raman spectra showed the fingerprint modes E^1_{2g} and A_{1g} were gradually quenched as they increased the energy (up to 92 eV), and a redshift of the E^1_{2g} mode. They prepared a FET device with their treated samples and by the measurements concluded monolayer MoS_2 can be tuned from a semiconducting to a metallic-like behavior.

[2]Deep trap state is a possible electronic state that requires an amount of energy relatively larger than the ambient thermal energy kT to be promoted to the conduction or valence band.

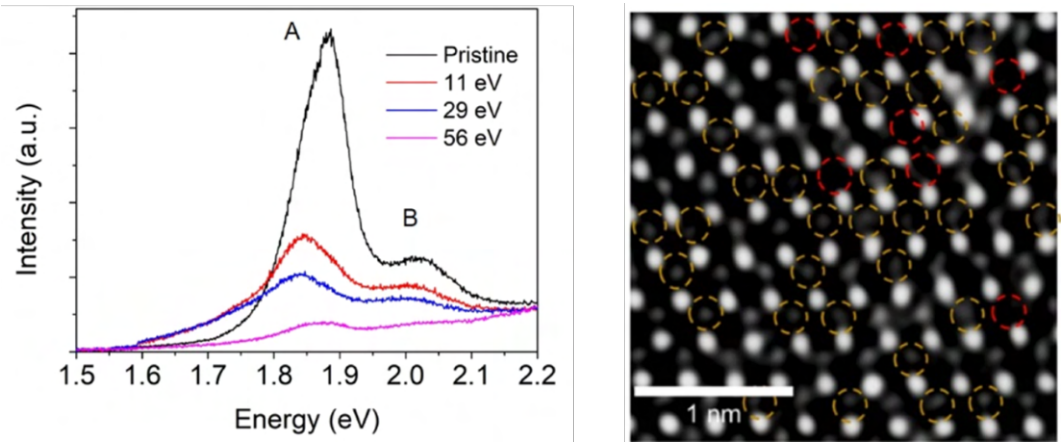

Figure 3.2: PL spectra for different helium ions energies (time fixed at 10 min); ADF-STEM images of monolayer MoS_2 sputtered with 56 eV helium ions for 10 min. The yellow and red circles denote monosulfur vacancies (VS) and disulfur vacancies (VS_2), respectively. Adapted from [52].

Parida *et al.* also attempted to tune the electronic and vibrational properties of large scale monolayer MoS_2 using a Helium ion beam [53]. The MoS_2 films were synthesized on 2-inch diameter c-plane sapphire substrates using gas precursors with MOCVD technique. The samples were irradiated with an ion implanter using $^4He^+$ with an energy of $8 \cdot 10^{-15}$ J (50 KeV). The working pressure was $2.8 \cdot 10^{-4}$ Pa ($2.1 \cdot 10^{-7}$ Torr) and the ion fluences ranged from $1.36 \cdot 10^{15}$ to $2.72 \cdot 10^{16}$ ions cm^{-2}. As shown in figure 3.3, the authors observed in the PL emission spectra a quenching in the A exciton in the samples treated; additionally they observed the apparition of a new feature, a bound exciton X_b around 1.7 eV (measured at 4 K), which they attribute to the formation of point defects. At beam fluence of $6.80 \cdot 10^{15}$ ions cm^{-2} (0.01 dpa) the authors suggest the bright peak may be the result of unique synergistic effects between lattice defects.

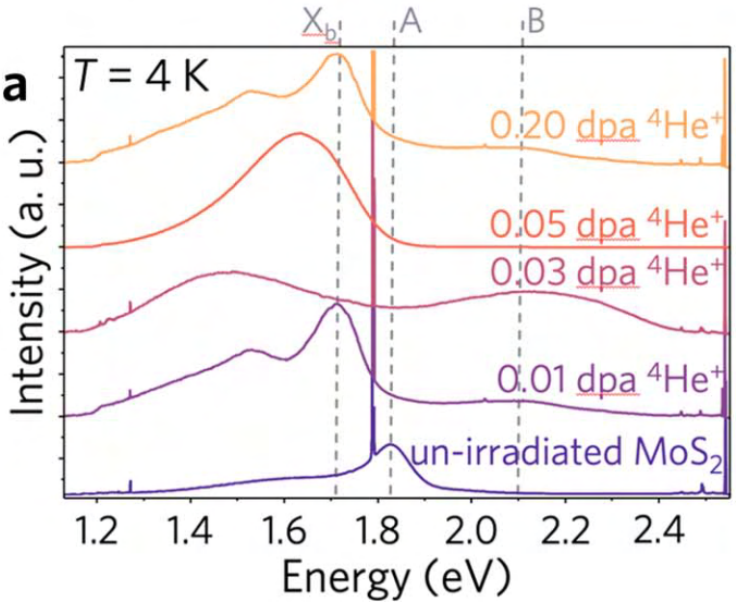

Figure 3.3: PL spectra of MoS_2 irradiated by $^4He^+$ ion beams with different fluences given in displacements per atom (dpa) show emergence of the bound exciton, X_b , peak around 1.7 eV upon irradiation attributed to generation of point lattice defects. Spectra are shown normalized to the intensity of sapphire peaks and were recorded at 4 K. Adapted from [53].

From these some relevant aspects stand out. The gas species selected to modify 2D MoS_2 is relevant, since it is able to react with the material like Oxygen, or it is less able to remove Sulfur and Molybdenum atoms, like Helium. The energy dispensed to create the ion beams (or plasma) also determines the treatment intensity per unit of time, rendering its control of great importance. The treatment time is an important parameter as it ultimately defines the ion dose received by the treated structures. What is less highlighted in general, but is of equal importance is the experiment's geometry, the ion source-to-sample distance, and the working pressure which influences the ions density. The creation of point defects in monolayer MoS_2 can increase photoluminescence through different mechanisms: they can introduce localized electronic states within the bandgap (either close to the valence band or the conduction band), thus facilitating the radiative transition; they can promote charge transfer between the defect sites and the crystal lattice, thus altering the electronic band and eventually facilitating the radiative emission; the defect sites can also create localized excitons (as seen in [53]) that enhance the PL emission; the modification of the band structure can also increase the light absorption, increasing the quantity of electron-hole pairs and thus the PL emission.

4
Proposal

Among the Two-dimensional Transition Metal Dichalcogenides representatives this work concerns monolayer MoS_2. The aim of this thesis is to enhance its Photoluminescence (PL) emission in comparison to its unaltered emission. The motivation is that enhancing monolayer MoS_2 photoluminescence emission can be beneficial for various applications such as optoelectronic devices, gas sensors, and photodetectors. Improved emission intensity can lead to higher sensitivity, better signal-to-noise ratios, and increased efficiency in these devices, increasing their performance and functionality.

In order to achieve this, low energy ion treatments will be applied to CVD grown monolayer MoS_2, following the task roadmap bellow:

- To synthesize 2D MoS_2 monolayer structures: Chemical Vapor Deposition (CVD) will be used. This comprises a process of optimization regarding the experiment's geometry, gas flow, precursors quantities, temperature used, and the temperature increase and decrease curves (ramps);
- Photoluminescence spectroscopy characterization: to evaluate the emission profile of the CVD grown samples. Structures with consistent PL emission are needed for reliable comparison;
- Raman spectroscopy: to determine the vibrational modes featured in the synthesized samples and verify if any significant change regarding defects in the crystal lattice occurs;
- Atomic Force Microscopy (AFM) measurements: to assess the structures' topography and its general features;
- To modify the MoS_2 surface applying ion treatments in a controllable manner;
- To repeat the characterizations and check out the applied treatments influence.

The objective is to find a fast way to modify the CVD grown monolayer MoS_2 surface and enhance its pristine PL signal by exploring a set of ion treatment parameters different from the covered in literature.

5
Part I: Nitrogen Plasma Treatment

This chapter describes in detail the experimental procedures adopted and results obtained during the first part of the thesis. All the experiments followed the same course of action: MoS_2 synthesis via CVD, sample characterization, subsequent treatment, after-treatment characterization, and data analysis. However, there are some differences between parts I and II which demonstrates the evolution of the work. In Part I the monolayer samples were subjected to a low-power Nitrogen gas plasma in order to enhance its photoluminescence. In Part II - for reasons that will become clear later on the text - the treatment applied was a Helium Ion Beam. Each part is subdivided in various tasks with a common core disclosed below.

The results presented in this chapter are published in *Vibrational Spectroscopy, 123:103454, 2022* [54].

5.1
Experimental Methods

5.1.1
MoS_2 synthesis

The substrates used to grow MoS_2 samples on were commercially available microelectronics-graded SiO_2/Si, with a 300 nm thick SiO_2 layer for good contrast under an optical microscope and for preventing chemical reactions between the sample and the substrate (i.e. sulfurization of silicon). They were cut in rectangular-like shapes of about 1 cm x 1.5 cm with aid of metallic tweezers, then subjected to an ultrasonic cleaner in ten minutes rounds submerged in acetone, isopropylic alcohol, and deionized water, in this particular order. Before usage the substrates were dried with a nitrogen gas blower.

The MoS_2 growth utilized NaBr as a salt assistant to the process, a modified version of the route previously used in the group by Safeer *et al.* [55]. The solid precursors used were 99.97 % pure MoO_3 powder and 99.5 % pure sulfur powder (both acquired from Sigma-Aldrich). The MoO_3/NaBr ratio used was 10, the powders were mixed before usage. The growth temperature was 1023 K while the sulfur source temperature was kept in 473 K. The precursor masses used were 4 mg and 200 mg for MoO_3 and Sulfur powders, respectively. This method yielded more monolayer structures along the substrate in comparison to salt absent experiments using the same parameters.

In the CVD setup installed, a furnace with a single heating zone was used (figure 5.1). The precursors were loaded in alumina crucibles in different quantities to optimize the growth process. Inside the Mo-source crucible clean substrates were placed diagonally with the SiO_2 layer facing down. A quartz tube with diameter of 25 mm was placed inside a cylindrical oven able to reach up to 1473 K. Both crucibles were placed inside the tube, the one containing the substrate was placed in the central region and the one loaded with Sulfur powder was placed 22 cm away. This tube was then connected to an Argon gas (Air Liquide, 5.0 purity) line, where a mass-flow controller (MKS 247C) was used to set a 100 sccm flow value. The transisiton-metal source was centered in the oven while the chalcogen source was placed upstream. Since the oven used had only one heating stage, an additional heating belt was used around the crucible containing Sulfur, being capable of reaching temperatures up to 573 K which were monitored by an external type K thermocouple and controlled with a electric current source. The growth window time was varied, being finally fixed in 10 minutes. The temperature rise ramp was set in 30 K/min, and the system cooled naturally afterwards. Both the furnace temperature ramp and the growth window were set by a Programmable Logic Controller (PLC). The heating belt was controlled manually at its current source.

Figure 5.1: The tubular furnace used to grow the samples and its controller.

5.1.2 Characterization

After synthesis, the samples were observed in an optical microscope (Zeiss Axio Scope.A1) using a x100 magnification to check how the growth procedure developed.

After a successful growth, the samples were characterized on a spectrometer integrated with an atomic force microscope (NT-MDT NTEGRA SPEC-

TRA, shown in figure 5.2) that was used to perform Raman Spectroscopy, Photoluminescence Spectroscopy, and Atomic Force Microscopy. This spectrometer is equipped with charge-coupled device (CCD) detector cooled down to around 204 K. It has a focal length of 52 cm and a photo-multiplier tube in the optical circuit to perfect the laser focus on the sample. The excitation wavelength used for resonance Raman spectroscopy was 632.8 nm generated by a He-Ne laser with a nominal power of 21 mW. The spectra were obtained using an 1800 lines/mm diffraction grating and a spectral resolution of 0.6 cm^{-1}. The acquisition time for Raman spectra was 2 minutes.

The atomic force microscopy (AFM) topographic images were taken in semi-contact mode, using a piezoelectric ceramic capable of moving within a 100 μm x 100 μm maximum area. The ceramic was set in a constant scan velocity of 20 μm/s regardless of the covered area. In this case, greater scanning velocities yielded worse image quality. The AFM images were produced with a 512 pixels x 512 pixels resolution. These data were treated via software (Gwyddion, [56]) to obtain the step height from the flat substrate surface to the MoS_2 samples and confirm if they were monolayers.

Photoluminescence spectra were obtained using a solid-state laser, which produced an excitation wavelength of 473.2 nm with a nominal peak power of 50 mW using a 150 lines/mm grating and a spectral resolution of 4 meV.

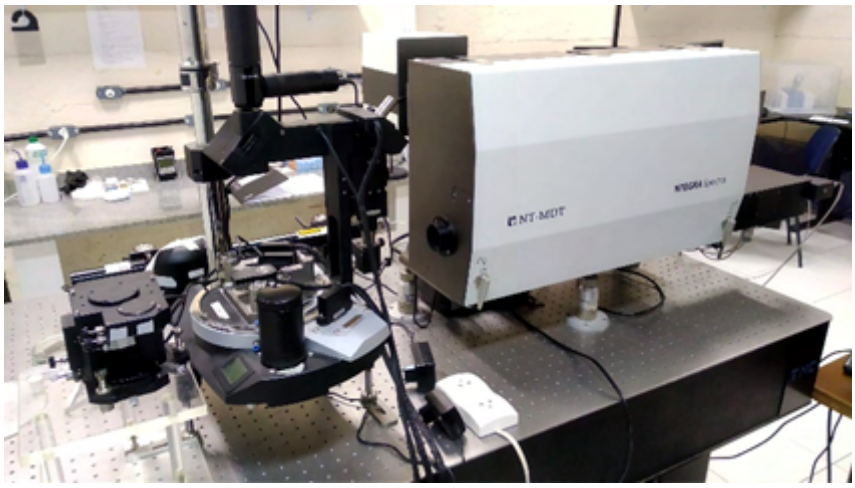

Figure 5.2: The NT-MDT NTEGRA SPECTRA spectrometer used.

5.1.3 Nitrogen Plasma Treatment

After characterization the synthesized samples were loaded into a comercial plasma cleaner system (Harrick Plasma PDC-32G-2 RF), shown in figure 5.3. This machine generates cold plasma using an RF coil with a power of 6.8 W (in the setting used). It is important to notice this is not the power density

delivered to the sample, which is highly dependent on the working pressure. A dry scroll pump was used to achieve a base pressure of approximately 4.0 Pa inside the plasma cleaner chamber, then it was purged with N_2 gas for 60 seconds and evacuated down to the base pressure to remove residual air moisture and contaminants. Subsequently, N_2 gas (99,99 % pure from White Martins) was carefully injected through a needle valve into the chamber to maintain a constant pressure of 133.3 Pa (1 Torr). The treatment times tested were from 0 to 8 s with a 2-s step. After the treatment the chamber was purged back to atmospheric pressure and the samples stored in a low-vacuum environment.

Figure 5.3: The Harrick Plasma PDC-32G-2 RF plasma system used to treat the MoS_2 samples.

Finally, the treated samples were again characterized to check changes in their Raman spectra, PL emission, and topography.

5.2 Results

Figure 5.4 shows an optical microscope image of the grown monolayer MoS_2. In this representative image the triangular structures are the grown material and the back ground in contrast is the SiO_2/Si substrate. Some smaller dots of material can be seen all over the sample, these are residues of MoO_x reminiscent from the CVD process. The yellow region is the same scanned region used for PL maps in Figure 5.7.

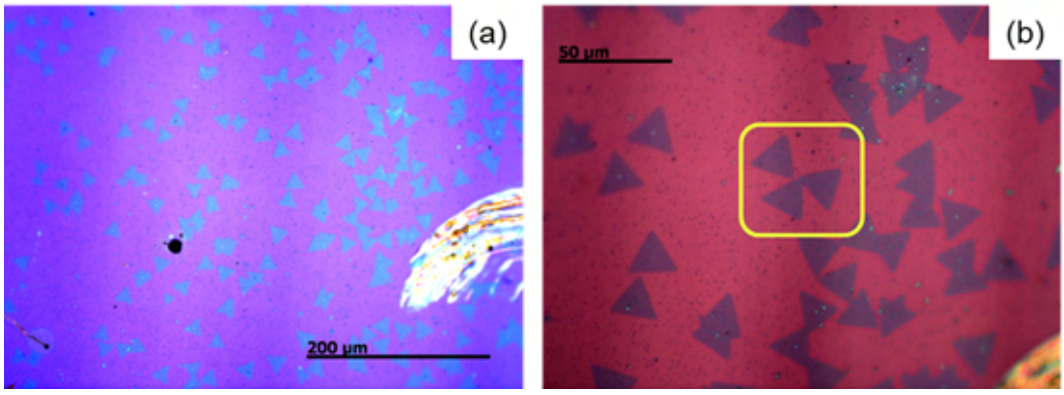

Figure 5.4: Optical micrographs of the grown monolayer triangles. The scale bars are (a) 200 μm and (b) 50 μm.

5.2.1 Atomic Force Microscopy

Figures 5.5 show representative atomic force micrographs of: (A) a pristine monolayer sample and (B) the same sample after a 8-s treatment, which was the longest time in this series. It is possible to see that the flakes shapes and sizes are not modified by the nitrogen plasma on a nanometer scale. These results show that the treatment applied did not destroy the MoS_2 flakes.

Due to the nature of the growth process some residues are present. These residues are scattered over the surface of the monolayer triangles and the substrate, shown in figures 5.5 (A) and (B). This phenomenon was commonly observed when performing MoS_2 growth via CVD, other TMDs like WS_2 present a cleaner deposition comparatively [57].

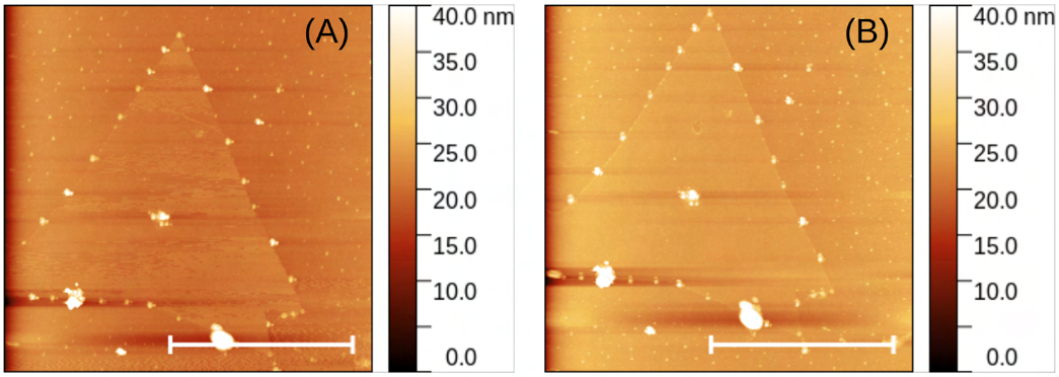

Figure 5.5: (A) A representative topographic micrograph of a pristine MoS_2 monolayer sample and (B) the same sample after 8 s treatment. The scale bar in (A) and (B) is 5 μm.

Figure 5.6 shows a representative step profile highlighting the average height of the CVD grown structures; the MoS_2 crystals are 0.8 $\pm$ 0.2 nm in

height compared to the SiO_2 substrate flat surface. This value is comparable to other observations in literature [58, 59].

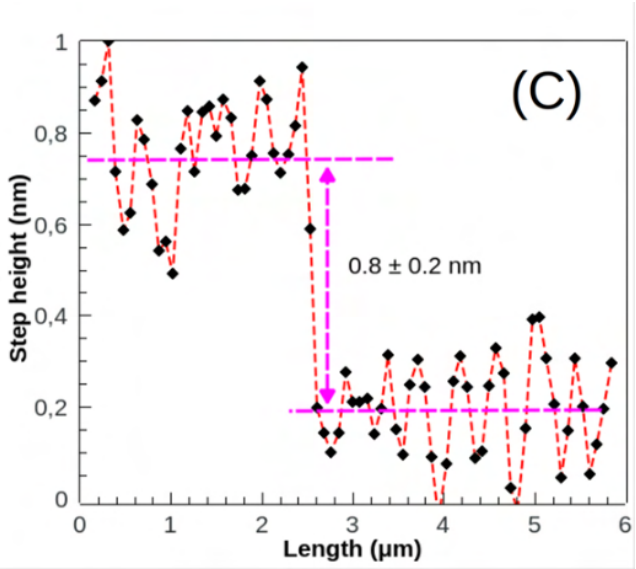

Figure 5.6: Profile showing the MoS_2 monolayer step height.

5.2.2 Photoluminescence Spectroscopy

Figures 5.7 and show the photoluminescence (PL) maps of (A) pristine and (B) the same sample after 8 s of N_2 plasma treatment. A general decrease in PL instensity can be observed. This PL quenching behavior was observed in all the treated samples, regardless of time exposure.

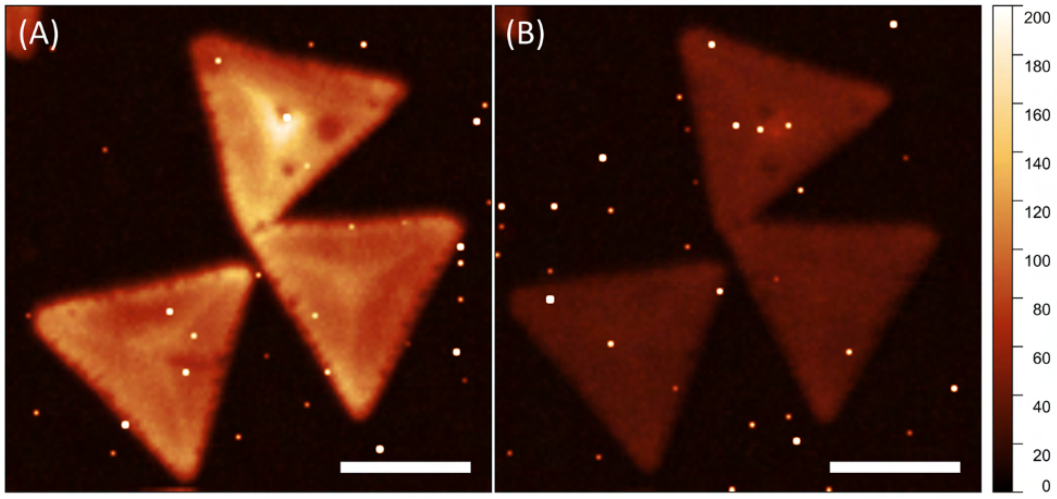

Figure 5.7: Photoluminescence maps on (A) pristine MoS_2 monolayers and (B) 8 s plasma-treated sample. The scale bar in figures (A) and (B) is 10 μm

The effect of N_2 plasma treatment caused the PL signal to drop as a function of the treatment time, as shown in figure 5.8. The observed intensity

drop was compared to the Si Raman peak, and this signal quenching from the pristine to the 8 s plasma-treated sample was approximately 76%. Additionally, and a small 30 meV redshift was observed from the pristine to the 8 s treated sample.

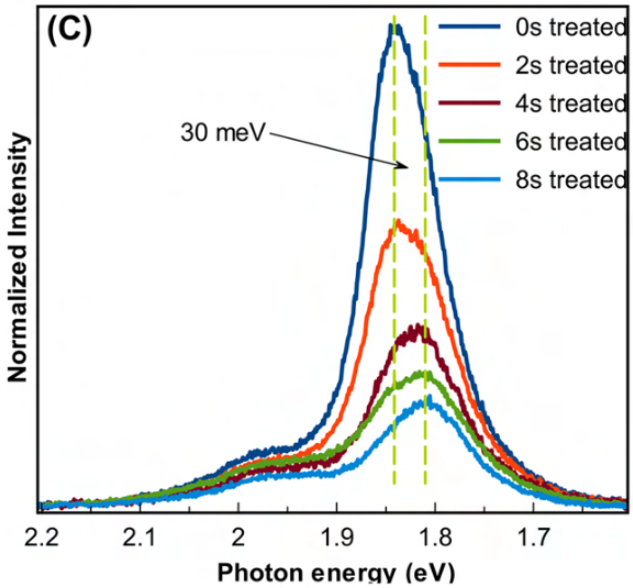

Figure 5.8: PL intensity as a function of incident photon energy for different treatment times. It is possible to see a 76% intensity quenching and a 30 meV peak redshift.

This redshift is not a consequence of the main A^0 excitation redshift but rather a change to the line shape due to different exciton contributions. Figures 5.9 show the photoluminescence (PL) peak deconvolutions of the (A) pristine, (B) 4 s, and (C) 8 s plasma-treated samples, respectively. The A^0 exciton emission energy was 1.85 eV, B exciton showed a peak maximum at 1.99 eV, and negatively charged A^- trion was centered at 1.81 eV. The A^0/A^- exciton intensity ratio dropped from 1.7 to 0.3 on average for several different monolayer structures. The line shape of the samples treated for 4, 6, and 8 s were dominated by the A^- emission peak, which explains the apparent redshift of the PL peak.

Studies with MoS_2 and WS_2 monolayers treated with N_2 and O_2 plasmas [49, 43, 60] suggest this kind of treatment might generate a change in the acceptor/donor density in the bandgap of the material, pointing to doping process occurring in the treated monolayers. The broadening of the A^0 exciton full width at half maximum (FWHM) observed (table 5.1) is an evidence of the loss of homogeneity of the samples due to the increase in defects responsible for the reduction of exciton lifetimes. This loss of homogeneity could also be caused by a nitrogen doping contribution.

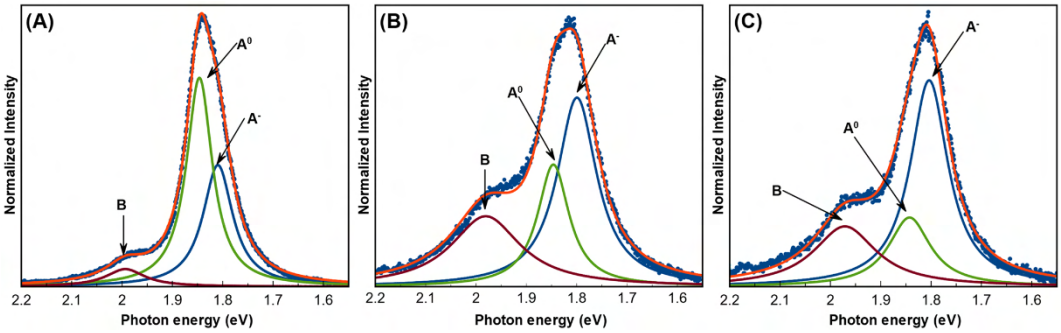

Figure 5.9: PL intensity as a function of incident photon energy and A^0, B, and A^- PL peak contributions of (A) pristine, (B) 4 s treated, and (C) 8 s treated samples.

Treatment time (s)	A^0 FWHM (meV)	A^- FWHM (meV)	B FWHM (meV)	A^0/A^- intensity ratio
0	31	36	46	1.7
2	31	31	69	1.6
4	38	48	83	0.6
6	41	44	76	0.6
8	50	46	75	0.3

Table 5.1: Photoluminescence fitted peak parameters evolution as a function of the treatment time.

5.2.3 Raman Spectroscopy

Figure 5.10 shows the nearly resonant excitation (633 nm) Raman spectra of the pristine, 2, 4, 6, and 8 s plasma-treated MoS_2 monolayers. Several modes are observed in comparison to a non-resonant (473 nm) spectrum of the same sample, as shown in figure 5.11, where only the A_1' and E′ modes are present [61]. In these accumulated spectra is observed that the luminescence background significantly decreases because of the creation of defects in the crystals. Off-resonance Raman spectroscopy did not show any relevant spectral shift of the main A_1' and E′ phonons for up to 4 s, as shown in Figure 5.11, and remained at 380 cm^{-1} and 399 cm^{-1}, respectively. For 8 s of treatment a 2 cm^{-1} blueshift in A_1' and a 2 cm^{-1} redshift in E′ modes was observed. These shifts observed in the 8 s treated samples are related to some amount of p-doping and strain taking place [47]. Nitrogen doping was indeed predicted to induce p-type behavior [62, 63].

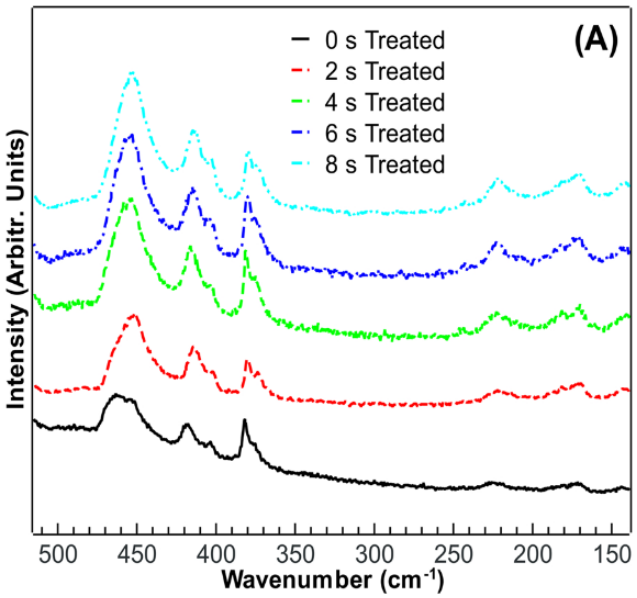

Figure 5.10: Accumulated Resonant Raman Spectra of monolayer MoS_2 treated with N_2 plasma in different times.

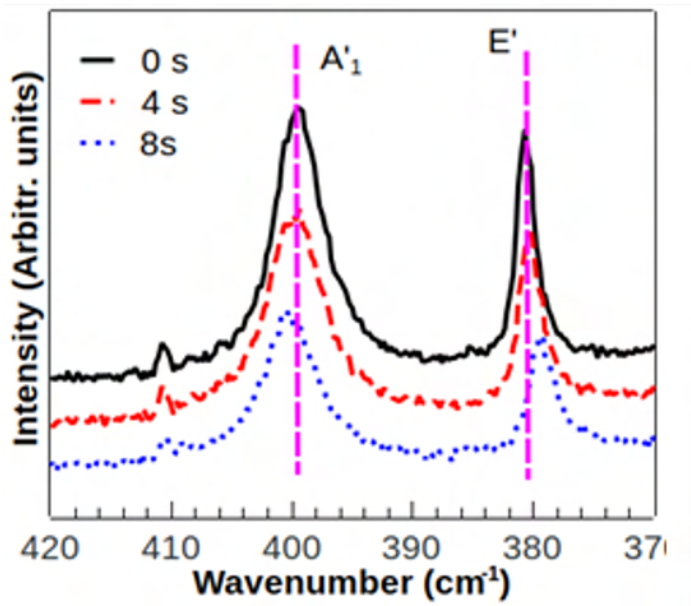

Figure 5.11: Raman spectra of pristine, 4 s treated, and 8 s treated MoS_2 monolayer structures using an excitation laser with 473.2 nm wavelength. Spectra acquired using an echelon grating with a spectral resolution of 0.4 cm^{-1}.

In order to quantify and analyze different regions of the Raman spectra, the luminescence background was subtracted considering a parabolic line shape, which is more suitable than using a linear one since the low-wavenumber part of the spectra experienced a slight gain because the excitation laser was not completely filtered out. The peak assignment used followed the approach discussed by Carvalho *et al.* [64]. For the fitting procedure fixed values for

the peak positions were imposed, leaving both the intensity and FWHM free. Figure 5.12 highlights the main spectral contributions close to the A_1' and E′ phonon modes for the pristine MoS_2 monolayers. Because of the use of a laser excitation energy close to the A^0 and B excitonic transition energies, other mode contributions are a consequence of regime intermixing. The peak at approximately 418 cm^{-1} in figures 5.12 and 5.13 is the result of the combination of second-order longitudinal acoustic (LA) and transverse acoustic (TA) phonons close to the K point of the Brillouin zone (BZ). Another prominent feature in this region was the broad peak between 420 and 500 cm^{-1}. This asymmetric band is referred to as the 2LA band in the literature. Indeed, the second-order 2LA(K) double resonant phonon mode contributes to the overall shape of this region; however, this line shape is a consequence of more complex phonon scattering processes. This region could be deconvolved into at least four contributions. The vibrational mode at 452 cm^{-1} is the is van Hove's singularity overtone peak [65, 66, 67]. The second and third peaks at 461 cm^{-1} and 467 cm^{-1}, respectively, are double resonant Raman processes related to the LA mode at the K and M points of the BZ.

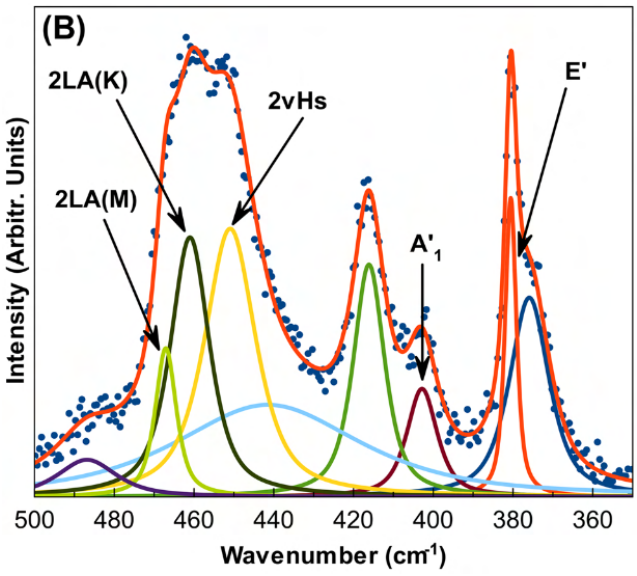

Figure 5.12: Peak deconvolution and assignment of the principal mode contributions of pristine samples.

Figure 5.13 shows the same deconvolution analysis and spectral features for the 8 s treated samples. There was a noticeable change of the "2LA band" contributions. Additionally, the in-plane E′ mode quenching was observed. This quenching is points towards a minor degradation the samples underwent during the treatment, which is expected, as seen in other studies in the literature [68].

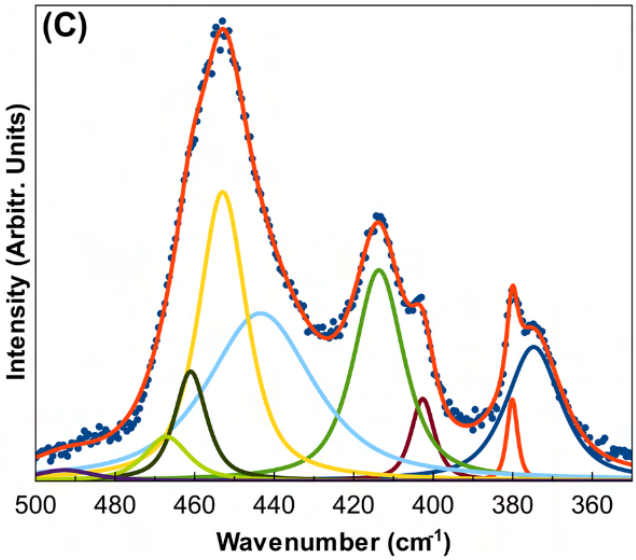

Figure 5.13: Raman spectrum of 8 s treated sample.

Figure 5.14 shows the evolution of the FWHM of the 2LA(K) and 2LA(M) modes as a function of the plasma treatment time. There is an apparent increase in the double resonant 2LA(M) FWHM values as the plasma creates more defects by either lattice vacancies or nitrogen substitutional doping. These defects behave as phonon scattering centers, and the FWHM increase indicates more phonon scattering events near the M point of the BZ due to the presence of more defects in the lattice [64, 60]. In contrast, the 2LA(K) mode loses intensity, and the FWHM decreases from 5.7 cm^{-1} to around 4.8 cm^{-1}. This decrease is within the experimental errors, hence it might be in reality constant. The observed behavior of these modes highlights how one can qualitatively discriminate monolayers by their density of defects by analyzing the FWHM of such spectroscopic features.

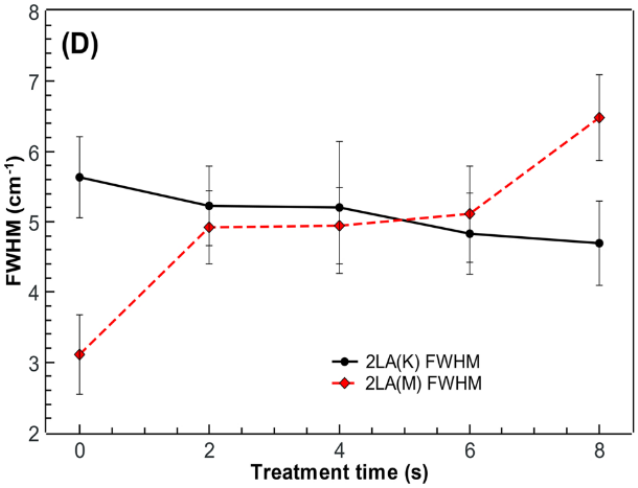

Figure 5.14: Behavior of the 2LA(K) and 2LA(M) modes FWHM.

The analysis of lower-wavenumber phonon modes at the 190–260 cm^{-1} can be used to quantify and discriminate samples with either a higher or lower density of defects, as the peak at around 220 cm^{-1} is essentially a convolution of longitudinal acoustic modes directed to the K and M points of the BZ. Contrasting with what has been shown in similar works regarding the defect creation on WS_2 monolayers [69], the lower signal-to-noise ratio prevents the precise determination of the position of such modes. There is no noticeable change in the spectra, except for the low intensity of the peaks in this region, observed for pristine samples due to their apparent lower density of defects, which is significantly higher in the treated samples. Five Gaussian-Lorentzian curves corresponding to the first-order contribution of the LA(K) and LA(M) phonons were assigned, along with another two at a lower wavenumber.

Ideally, MoS_2 samples without defects would prevent the observation of LA modes, as the momentum conservation condition cannot be satisfied by phonons scattered away from the BZ center. On the other hand, defects are intrinsic to the material when synthesized by chemical vapor deposition (CVD) and BZ edge modes can be observed using conventional Raman measurements. The selection rules are further relaxed under resonant Raman spectroscopy conditions. Figure 5.15 shows the lower wavenumber of the pristine sample Raman spectrum, and figure 5.16 shows the 8 s plasma-treated sample. There is an intensity decrease in LA(K) due to the treatment.

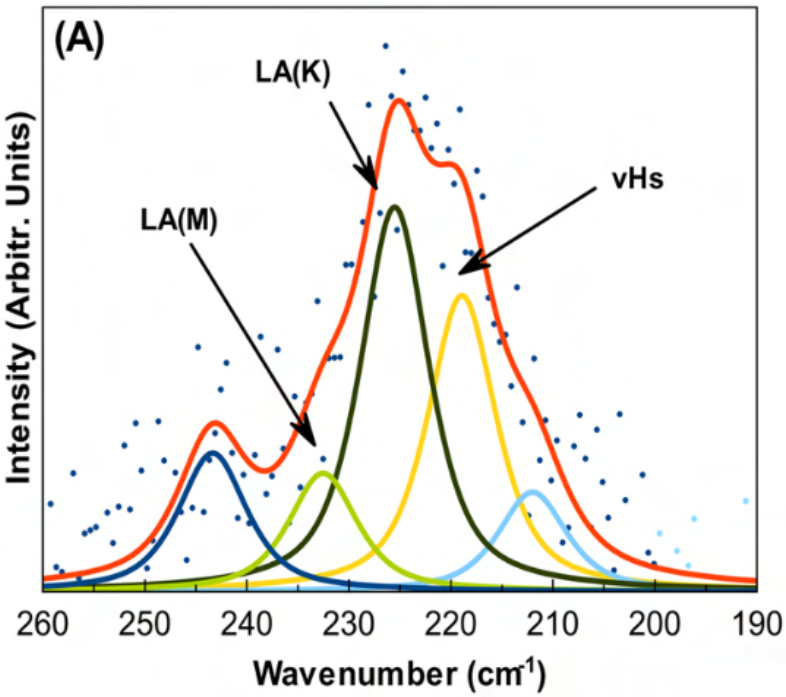

Figure 5.15: Raman spectra of the low wavenumber region of pristine MoS_2 monolayer.

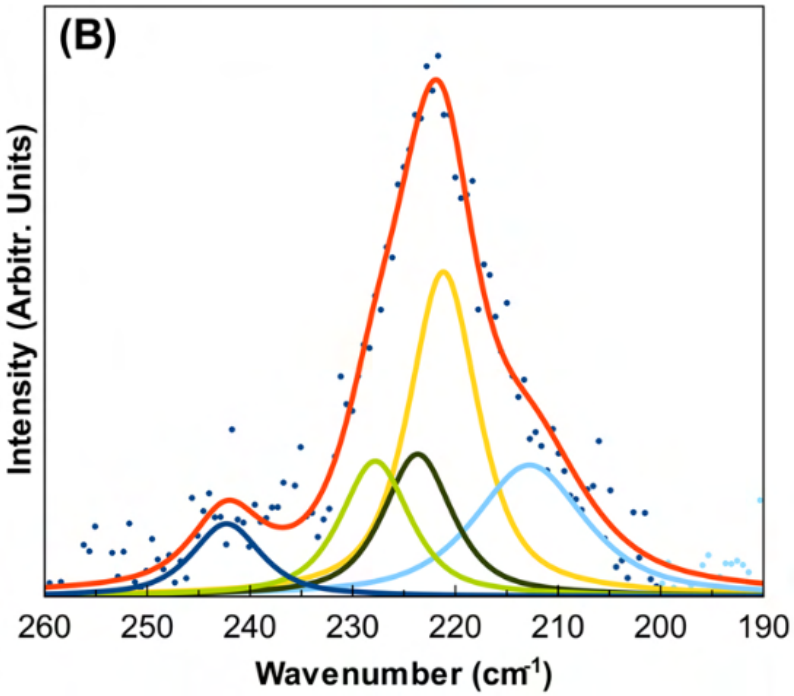

Figure 5.16: Raman spectra of the low wavenumber region of 8 s treated MoS_2 monolayer.

Figure 5.17 shows the intensity ratio variation of $I_{LA(M)}/_{LA(K)}$ due to the treatment process. This relative intensity may indicate more defects in the samples and shows that the 2LA(M) and 2LA(K) FWHM results are consistent. This may be due to the scattering increment in the M point of the BZ, where, in contrast to the LA(K) mode, shows an overall relative intensity increase, as shown by the $I_{LA(M)}/I_{LA(K)}$ intensity ratio. This may be used as a qualitative indicator of the higher density of defects in the lattice. A similar approach was used to quantify defects considering the $I_{LA(M)}/I_{LA(E')}$ ratio [70].

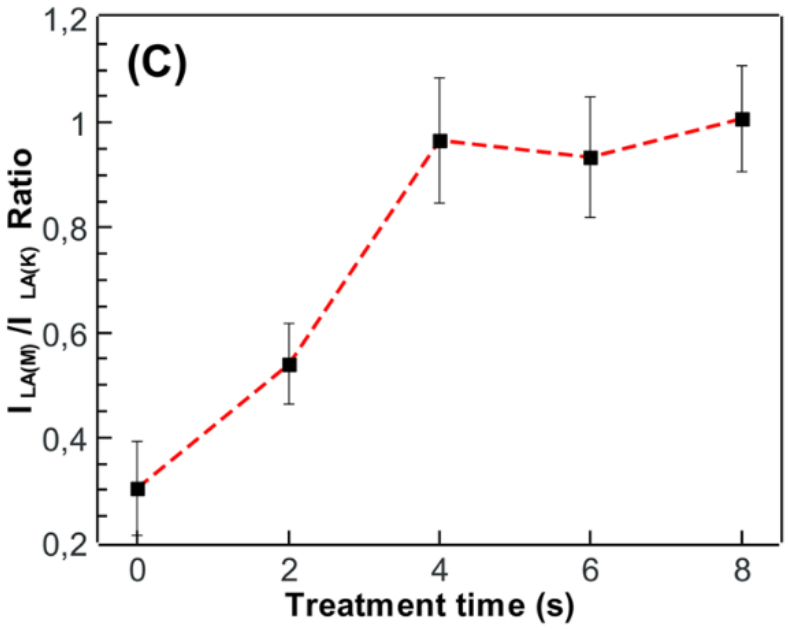

Figure 5.17: $I_{LA(M)}/I_{LA(K)}$ intensity ratio variation as a function of treatment time.

5.3 Discussion and Conclusions

In this first part of the thesis, this work did not reach the initial goal of increasing the PL emission of the MoS_2 monolayer using the Nitrogen plasma treatment. However, some valuable insight was gathered during these experiments and its results are non-neglegible. First, the AFM analysis not only confirmed the samples are indeed monolayered, but also they remain intact in a nanometer scale after treatment. Additionally, the very process of CVD must be improved if this should be the technique employed to fabricate devices for environments outside of laboratorial research, else more reliable techniques should be used regarding reproducibility and intermediate oxides debris. The PL analysis demonstrated the level of defects this treatment is able to impose in the samples is not small. This can be observed by the change in PL peak position due to the presence of more trions in the samples, meaning more defects as sulfur vacancies lead to more electrons being available to form such structures. The resonant Raman spectra analyses verified an evolution of key spectroscopic features, namely the quenching of the E' mode, the increase in the 2LA(M) FWHM, and the $I_{LA(M)}/I_{LA(K)}$ intensity ratios. These may be used as a figure of merit to show an increase in the density of defects in MoS_2 monolayers. This is particularly useful when checking the change on PL intensity by the increase of trions is not possible (e.g., in heavily doped samples).

The knowledge acquired guided the choices made for designing a new experiment. The use of salt-assisted CVD growth proved to be very useful to increase the yield of MoS_2 monolayers along the substrate, but also the PL emission was greatly enhanced using NaBr in the synthesis. Although an interesting result by itself, unfortunately this enhancement was not uniform along the samples, or even along the same experiment, because the local concentration of salt varies and cannot be easily controlled. This is a concern that should be addressed. The energy the Nitrogen ions have in the plasma was not known, only the power distributed to the coil, and also it could not be fine tuned due to the equipment interface limitations. Hence, if the energy of the ions could be controlled in some way it would be relevant, to try to make this treatment less aggressive to the samples in order to enhance their PL emission. These concerns are addressed in Part II.

6
Part II: Helium Ion Beam Treatment

In Part I an enhancement of the Photoluminescence emission was not achieved, hence this Nitrogen plasma treatment was deemed too aggressive even with the minimal power available in the Plasma Cleaner being used. Given this fact in Part II it was decided to apply a more subtle treatment to the monolayer MoS_2, with the possibility to control the treatment energy. A new experiment was set up: the gas species used changed to Helium (an atom lighter than Nitrogen) and instead of a plasma generator, an ion source gun was used. Therefore, not only the treatment time was controlled, but also the energy with which the ions reach the sample surface. This chapter describes the experimental methods adopted and the results obtained.

6.1
Experimental methods

6.1.1
MoS_2 Synthesis

In order to grow the monolayer MoS_2 samples a Chemical Vapor Deposition (CVD) system was assembled inside a fume hood (figure 6.1), in a system different from the one used in Part I.

Figure 6.1: The CVD system mounted inside a fume hood used.

Unfortunately the use of salt was proven unreliable regarding reproduction and photoluminescence intensity, which is a phenomenon yet to be fully explored. Given this fact, in the second part of the project NaBr salt was not

used. The precursor masses used were 4 mg and 200 mg for MoO_3 and Sulfur powders, respectively. A furnace with a single heating zone was used. The precursors were loaded in alumina crucibles. Inside the Mo-source crucible clean substrates were placed diagonally with the SiO_2 layer facing down. A quartz tube with diameter of 25 mm was placed inside the furnace. The crucibles were placed inside the tube, the one containing the substrate was placed in the central region and the one loaded with Sulfur powder was placed 22 cm away. This tube was connected to an Argon gas (Air Liquide, 5.0 purity) line, where 100 sccm flow value was set. The transisiton-metal source was centered in the oven while the chalcogen source was placed upstream. A heating belt was used around the crucible containing Sulfur, where temperature was kept in 473 K. The growth window time was varied, being finally fixed in 10 minutes. The growth temperature had to increase to 1123 K to achieve MoS_2 nanostructures growth, and the temperature rise ramp was set in 30 K/min, and the system cooled naturally afterwards. Both the furnace temperature ramp and the growth window were set by a Programmable Logic Controller (PLC). The heating belt was controlled manually at its current source.

6.1.2 Helium Ion beam Treatment

The Ion Source (IQE 11/35 SPECS) used is able to control the energy that accelerates the ions up to 5 keV[1]. This system is mounted on a ultra-high vacuum chamber (figure 6.2), maintained at 10^{-5} Pa, where other experiments are also performed (e.g. X-Ray Photoelectron Spectroscopy). Before the treatment the Ion Source was degassed, being submitted to a potential difference between its plates to release any adsorbents on its surface. The gas line used to introduce Helium (99.99999% pure from White Martins) in the Ion Source was purged before each experiment, and a needle valve was used to set a working pressure of 4.5x10^{-3} Pa.

[1]Along the text the energy is expressed in eV for readability. The SI unit conversion factor is $1\ eV = 1.602176634 \cdot 10^{-19}\ J$ [71].

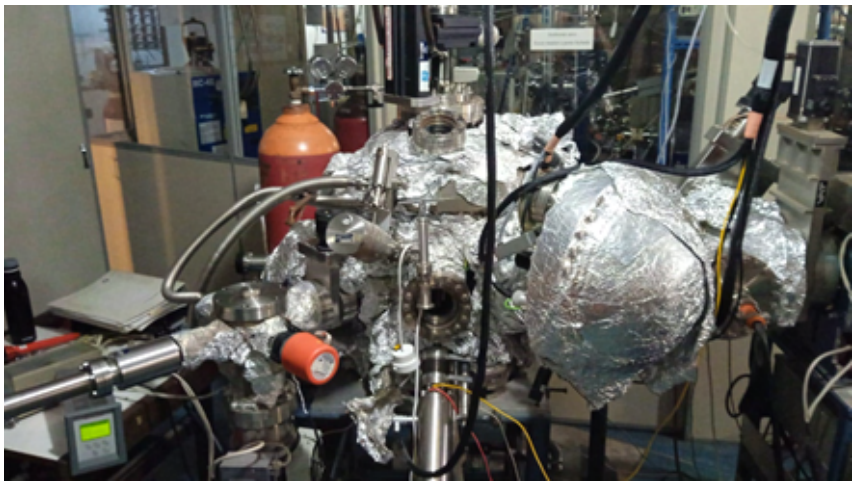

Figure 6.2: Ultra-high vacuum chamber where the Ion Source IQE 11/35 is installed.

During Part I, when applying a nitrogen plasma the number of ions reaching the sample surface per second per unit area was unknown, which is not ideal but was not a problem since it was a fixed number. The total dose distributed onto the sample was only a function of the treatment time. In this new experiment the energy varies, then the ion dose was measured for different energies to check its behavior. This was done preparing a circular copper foil with a measured area of 1.32 cm^2 supported by a plastic insulator substrate. This serves as an electrode to receive the incoming Helium ions, which is placed upon the sample-holder (but isolated from it with a phyllosilicate mineral foil, otherwise the whole sample-holder would become the electrode) and connected with a metallic arm, shown in figure 6.3. An open electric circuit is formed: the electrode, the connector cables at the sample-holder leading outside the vacuum chamber, and finally a series connected ammeter.

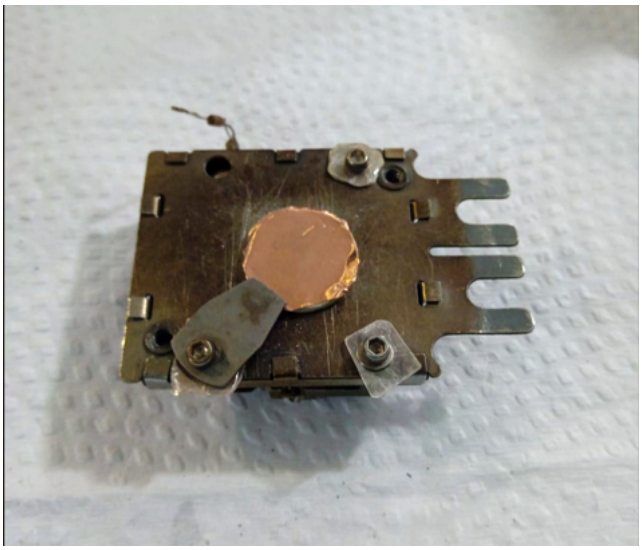

Figure 6.3: The copper foil electrode mounted on the sample-holder for ion dose measurement.

When the Ion Beam is turned on, the charges flow through the circuit and are read by the ammeter outside the chamber. The ion dose is computed using the equation $N/t = I/e$, where N/t is the number of ions per second, I is the measured current, and e is the electron charge. The resulting dose was measured for different energy values and then normalized by the electrode area. Figure 6.4 shows the Helium Ion dose per second per cm^2 for a fixed pressure of 4.5x10^{-3} Pa.

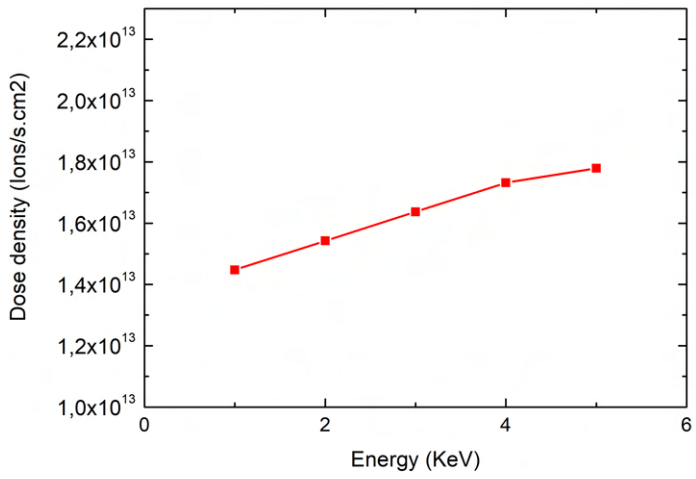

Figure 6.4: Helium ion dose density as a function of beam energy.

The samples were loaded inside a pre-chamber where a turbomolecular pump evacuated it to a pressure low enough not to contaminate the main chamber with particles from the outside atmosphere. Then the samples were

loaded inside the chamber and the sample-holder is positioned to a 90° angle to the Ion Source as projected in the entrance plane of the manipulator arm. Because of the chamber's fixed geometry and the limited degrees of freedom for the sample-holder there is still about a 30° angle of incidence of He ions in relation to the sample plane.

Two sets of experiments were performed. First, the Ion Beam energy was fixed at 5 KeV, while the time of exposure was varied, the times tested were 10, 20, 30, 60, 120, and 180 seconds. Then a certain time value was determined as optimal and fixed, while the energy was varied, the energies tested were 50, 300, 500, 1000, and 5000 eV.

Finally, the characterizations were once again performed to check the if any change occurred.

6.2 Results

Figure 6.5 shows representative optical micrographs of different MoS_2 samples grown in the CVD system implemented inside a fume hood for Part II. It is possible to see the growth yield is less than the salt-assisted process comparatively. In some samples multi-layer structures grew on top of monolayer structures, which can be distinguished by their different optical contrast. The square highlighted is also studied in the PL map shown in figure 6.13.

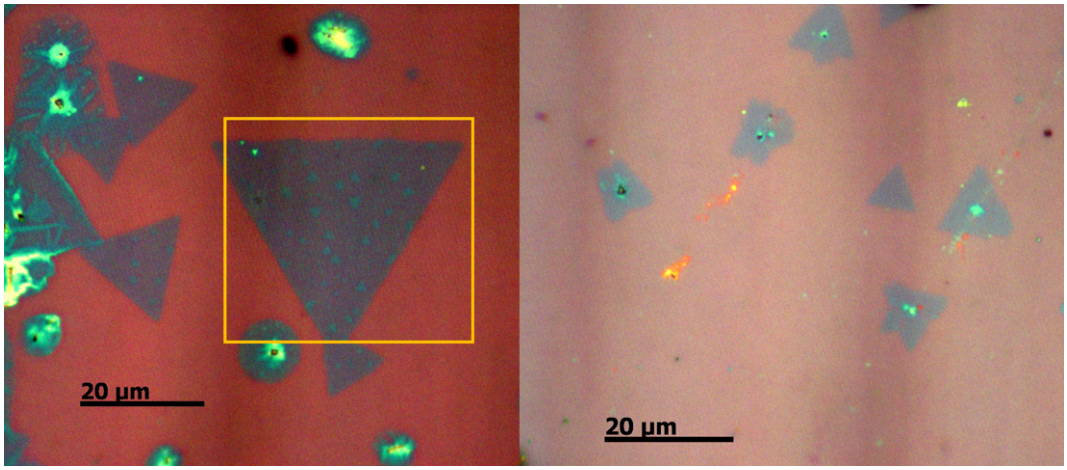

Figure 6.5: Optical microscope images of different samples of CVD grown MoS_2. The highlighted area is further investigated in the PL map depicted in figure 6.13.

6.2.1 Photoluminescence Spectroscopy

The solid-state laser with 473.2 nm excitation wavelength was substituted for a similar one with a 532 nm wavelength at this time, so all the PL spectra were collected using a 532 nm laser. In order to improve the characterization reliability when a spectrum was collected in a certain point on a sample its coordinate on the substrate was photographed and consulted after the treatment to guarantee the same spot would be measured again. The photoluminescence spectra taken before and after treatment were normalized to the Si Raman peak for intensity peak comparison. The non-treated sample PL emission peak was then normalized to 1, and the subsequent peak intensity change is displayed as a multiple of its original intensity. Because the samples vary slightly in their PL intensity and peak position due to growth process this approach was chosen to express the PL change more reliably. The results for the fixed energy value of 5 KeV are presented in figure 6.6, where the dashed line highlights the pristine PL intensity value of 1. It is possible to observe the exposure time had an influence in the PL emission intensity. The longer times tested from 1 to 3 minutes quenched significantly the signal intensity, and a treatment performed for 30 minutes (not displayed in figure 6.6) completely quenched the PL and Raman signals, showing the crystalline structure was completely destroyed is this extreme case. Treatments conducted for 20 and 30 seconds presented a slight decrease in the PL intensity. The 10 s treatment was the only time tested which enhanced the PL emission, which was the experiment objective and was considered a success. In the next series of experiments this time was fixed. These results contrast with Huang *et al.* [52] in the sense they did not achieve a PL enhancement, perhaps owing to the longer times used.

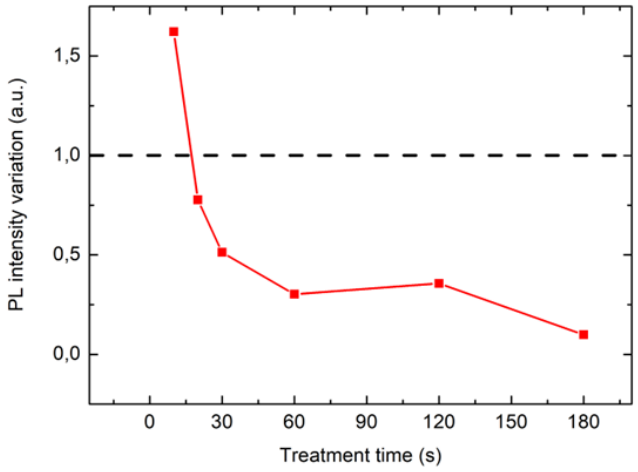

Figure 6.6: Photoluminescence peak intensity variation as a function of treatment time. The energy was fixed at 5 KeV.

Figure 6.7 shows the accumulated normalized PL signal intensities for different treatment times at fixed energy of 5 KeV as a function of emission wavelength. In this graph can be observed the emission peak varies slightly from one sample to another, but its overall shape is preserved. This observation contrasts what was observed by Parida *et al.* [53], where they observed the apparition of a new bound exciton while the pristine emission was quenched, possibly due to higher ion dose and energy applied. The graph in figure 6.7 by itself might lead one to think the Ion Beam treatment is causing considerable peak emission wavelength shifts. This is not completely true, because every particular sample has a different peak emission at its pristine form, a more concise way to observe a peak position change is to compare each treated sample to its pristine counterpart before the Ion Beam influence. These data are displayed in table 6.1, where it is possible to notice the peak deviation values were from 1 to 3 nm (which corresponds to a change in photon energy of about 0.1 eV), excluding the 60 s sample, which presented an anomaly in peak position both before and after treatment.

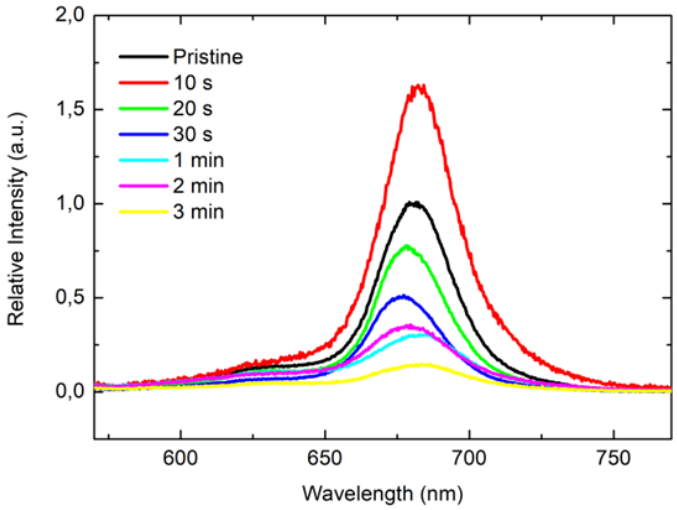

Figure 6.7: Monolayer MoS_2 accumulated normalized PL signal intensities for different treatment times at fixed energy of 5 KeV.

Treatment time (s)	Pristine PL peak position (nm)	Treated PL peak position (nm)	Position difference (nm)
10	680.52	682.18	1.66
20	678.20	679.20	1.00
30	677.53	676.54	-0.99
60	672.55	683.51	10.96
120	677.20	679.53	2.33
180	681.19	684.18	2.99

Table 6.1: Photoluminescence emission peak positions for samples treated with Helium Ion Beam for different times at fixed energy of 5 KeV.

In the first series of experiments only the 10 seconds treatment yielded an enhancement of the PL peak intensity. This time was then fixed for a second series where the energy was varied. Figure 6.8 shows the PL peak intensity relative to its pristine emission intensity prior to treatment as a function of energy. The behavior is more complex with changing energy values than observed when varying time, pointing that there must be an optimized energy value that maximizes the PL intensity for a given exposure time. Energies lower than 5 KeV were tested and the treatment with 500 eV was the optimal result, with an enhancement factor of 2.07 of normalized PL emission. Comparatively, the best result in the time variation series was an enhancement factor of 1.62. The treatments with energy 300 eV and 1 KeV reduced the PL intensity.

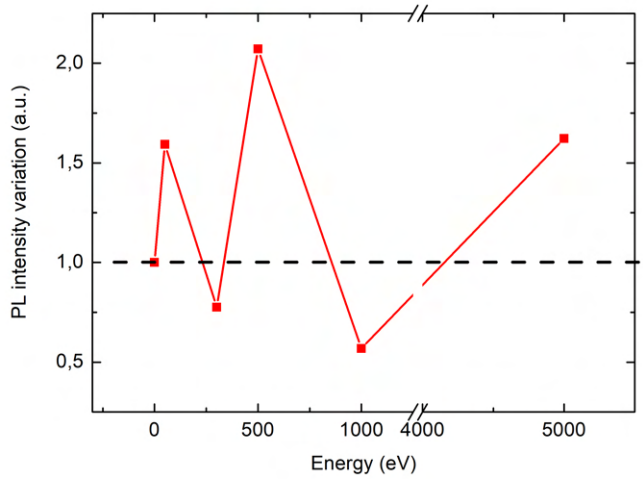

Figure 6.8: Photoluminescence peak intensity variation as a function of treatment energy. The time was fixed at 10 s.

Relative PL intensity signals for different energy values after treatment as a function of emission wavelength are displayed in figure 6.9. In table 6.2 are displayed the PL emission peak position differences after treatment in comparison to each pristine sample, again were verified changes in position up to around 3 nm (equivalent to a change in energy emission of about 0.1 eV).

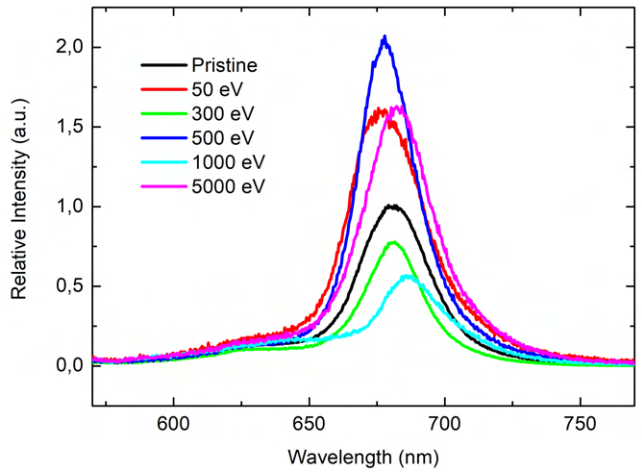

Figure 6.9: Monolayer MoS_2 accumulated normalized PL signal intensities for different treatment energies at fixed time of 10 s.

Treatment energy (eV)	Pristine PL peak position (nm)	Treated PL peak position (nm)	Position difference (nm)
50	676.87	676.87	0
300	677.87	681.19	3.32
500	677.87	680.52	2.65
1000	685.51	685.84	0.33
5000	680.52	682.18	1.66

Table 6.2: Photoluminescence emission peak positions for samples treated with Helium Ion Beam for different energies at fixed time of 10 s.

In this two series of experiments the objective of improving the PL emission signal of the MoS_2 was reached via the Helium Ion Beam treatment implemented. The best results are compiled in table 6.3 where the treatment parameters used and PL emission enhancement factor are shown.

Treatment time (s)	Treatment energy (eV)	PL emission enhancement factor
10	5000	1.62
10	500	2.07
10	50	1.59

Table 6.3: Helium Ion Beam treatment parameters and PL emission enhancement factor.

Figure 6.10 shows the PL emission peak deconvolution of the A and B excitons and the A^- trion on a pristine sample. It is possible to see that in CVD grown pristine samples the A exciton is the main feature, while the B exciton and the A^- trion have a minor contribution. Looking at a representative deconvolution of the best treatment of the time variation series (5 KeV beam for 10 s) displayed in figure 6.11 it is observed the trion contribution rises without becoming the main feature. This observation is different from what was seen in Part I, evidencing this treatment is indeeed less abrasive. The deconvoluted PL signal of the best treatment of the energy variaton series (500 eV beam for 10 s) shows the intensity of the trion contribution a increased even less (figure 6.12), which makes sense, since this treatment used 10 times less energy.

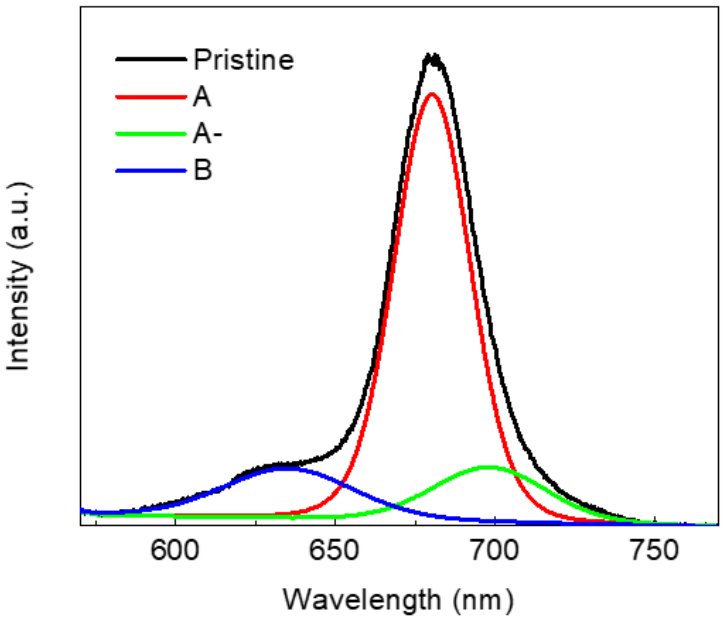

Figure 6.10: Photoluminescence emission spectrum of a pristine sample. Deconvolution showing the A and B excitons, and the A^- trion contributtions to the line shape.

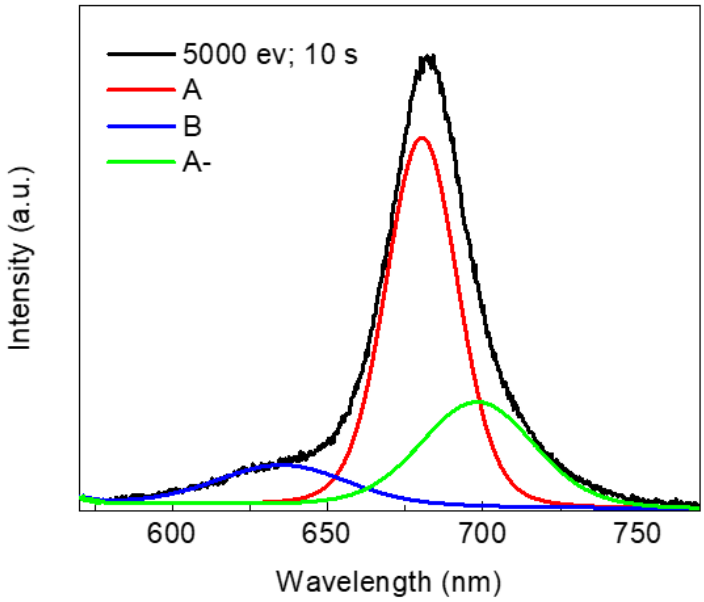

Figure 6.11: Photoluminescence emission spectrum of a sample treated for 10 s with a 5 KeV Helium ion beam. Deconvolution showing the A and B excitons, and the A^- trion contributtions to the line shape.

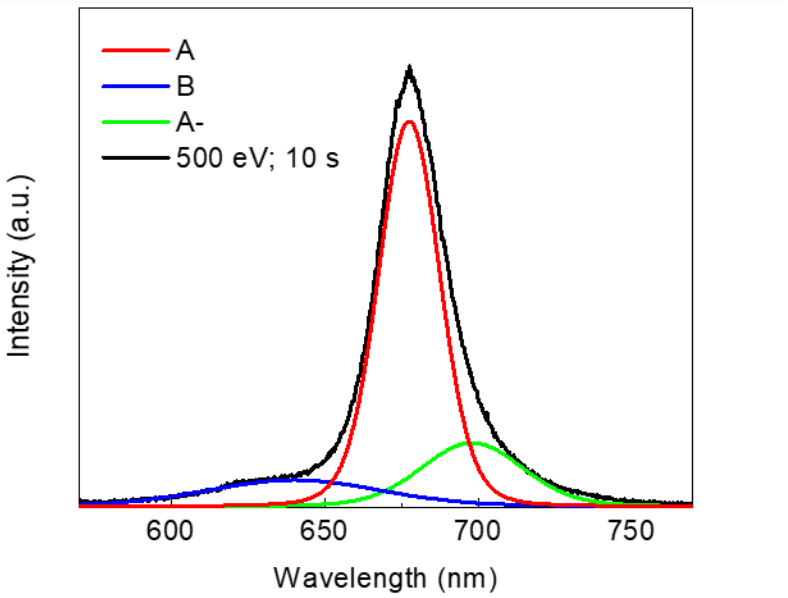

Figure 6.12: Photoluminescence emission spectrum of a sample 10 s with a 500 eV Helium ion beam. Deconvolution showing the A and B excitons, and the A^- trion contributtions to the line shape.

A PL map of a pristine sample and the same sample after being subjected to a 50 eV Helium beam for 10 s is shown in figure 6.13. These images are normalized to the Si Raman peak for comparison. It was observed an enhancement of the PL signal at the top of the triangular structure, but it was also observed a minor decrease at the bottom region, rendering the whole sample to a uniform PL signal. This observation was not unique and hints towards two conclusions. The first is not all samples are created equal due to the inability to control the synthesis process in its full extension, this is something that should be addressed when developing this process further for larger areas implementation. The second is the incident angle of ions is non-negligible, in such a way the fluence might not be constant if the sample —which is manually positioned—is not placed exactly in the same spot every experiment. The latter can be resolved by changing the geometry and the scale of the Ion Source when aiming to device fabrication. This was not observed in Part I because the Plasma Cleaner used a coil that delivered Nitrogen plasma omnidirectionally.

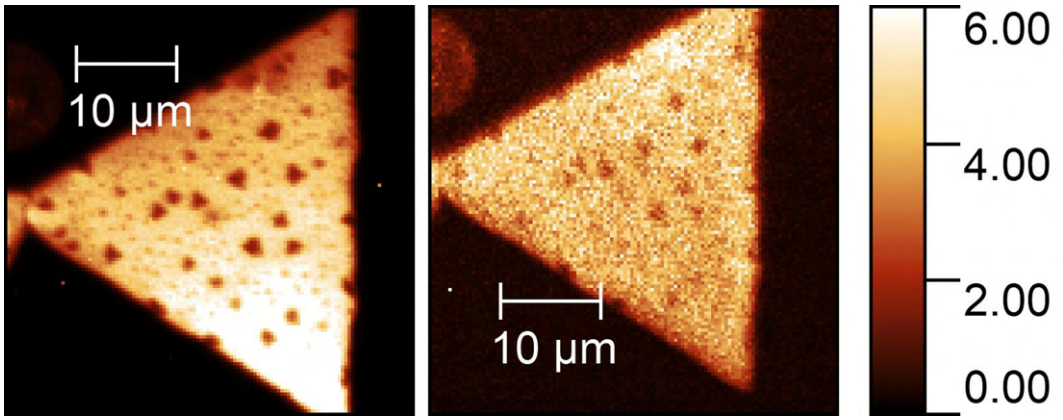

Figure 6.13: A pristine monolayer MoS_2 sample Photoluminescence map and the same sample after being subjected to a 50 eV Helium beam for 10 s.

Finally, figure 6.14 shows a pristine monolayer MoS_2 sample Photoluminescence map and the same sample after being subjected to a 500 eV Helium beam for 10 s, both images are normalized to the Si Raman peak for comparison. These were the treatment conditions found to enhance the PL signal the most. It can be observed this treatment was uniform across the sample.

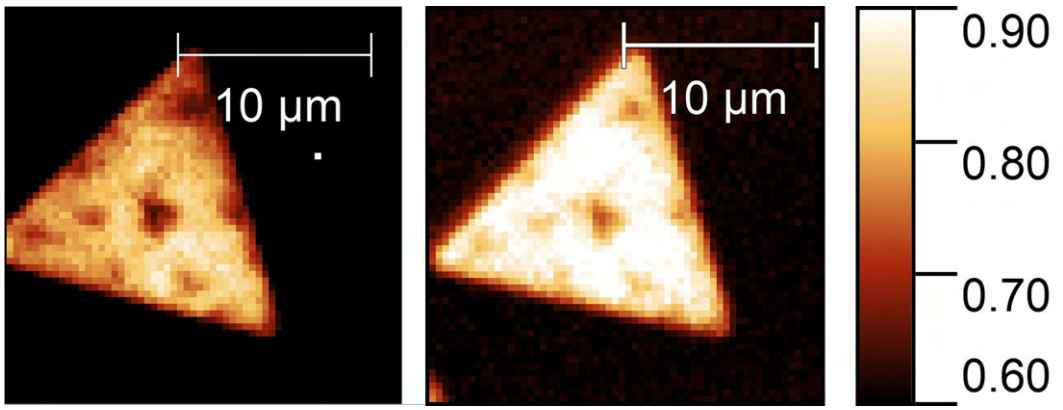

Figure 6.14: A pristine monolayer MoS_2 sample Photoluminescence map and the same sample after being subjected to a 500 eV Helium beam for 10 s.

6.2.2 Raman Spectroscopy

To analyse Raman spectra a combination of two softwares was employed (namely, Origin Pro and CasaXPS), where a parabolic baseline was removed from raw data and Gaussian-Lorentzian line shapes were used to fit the contributing vibrational modes. The spectra were calibrated to the Si Raman peak at 520 cm^{-1} and normalized to its intensity. The peaks positions were fixed whilst the intensity and FWHM were set free. Figure 6.15 shows the peak deconvolution and assignment of the principal mode contributions of pristine

samples before Helium Ion Beam treatment. One can observe the in-plane vibrational mode E′ at 380 cm^{-1} and the out-of-plane mode A_1' at 403 cm^{-1}, these are the first-order Raman peaks. The second-order peaks are located around 373 and 415 cm^{-1} and the "2LA band" in the 420–480 cm^{-1} region. This band comprises the 452 cm^{-1} second-order Van Hove Singularity peak; the 461 cm^{-1} 2LA(K) peak; the 467 cm^{-1} 2LA(M) peak; and a peak at 440 cm^{-1}.

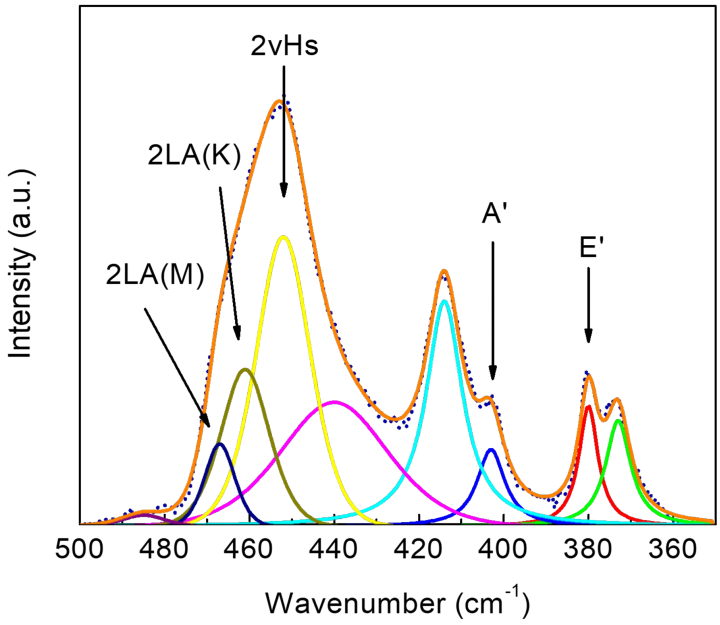

Figure 6.15: Peak deconvolution and assignment of the principal mode contributions of pristine samples before Helium Ion Beam treatment.

The most aggressive treatment performed used a 5 KeV energy beam for 3 minutes, for comparison its Raman spectrum is displayed in figure 6.16. The E′ and A_1' modes decreased in intensity, indicating the sample suffered some degradation in its crystal structure. This minor change for the most intense treatment is another evidence of how mild this approach is compared to others [45, 48, 54]. Additionally, with the energy of 5 KeV, the time that increased the PL signal was 10 s, and its corresponding Raman spectrum (figure 6.17) shows no relevant change in spectral features.

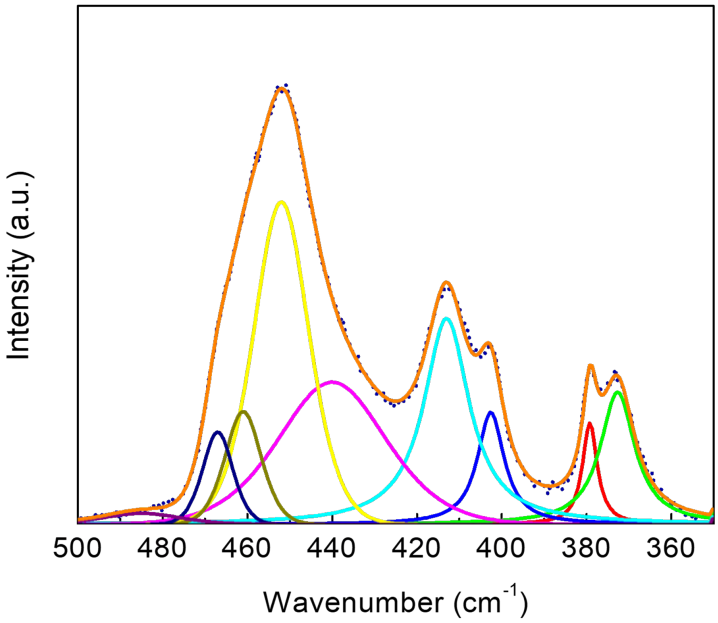

Figure 6.16: Peak deconvolution of the principal mode contributions of samples treated with 5 keV Helium Ion Beam for 3 minutes.

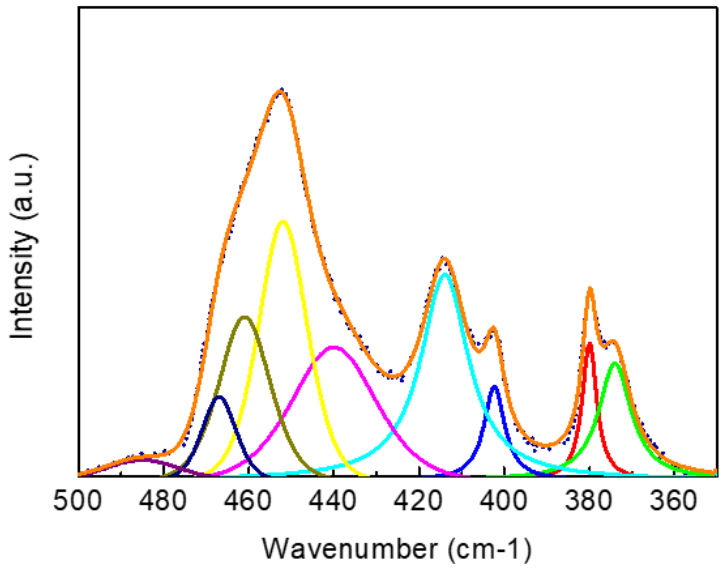

Figure 6.17: Peak deconvolution of the principal mode contributions of samples treated with 5 keV Helium Ion Beam for 10 seconds.

Considering the second order 2LA(M) peak FWHM, the change in its value after treatment as a function of time is represented in figure 6.18, not considering the 60 s sample which was not comparable by differing considerably in its pristine form. This shows this vibrational mode FWHM is almost

constant, meaning no change in crystallinity in this direction as opposed by the Nitrogen plasma of Part I (figure 5.14).

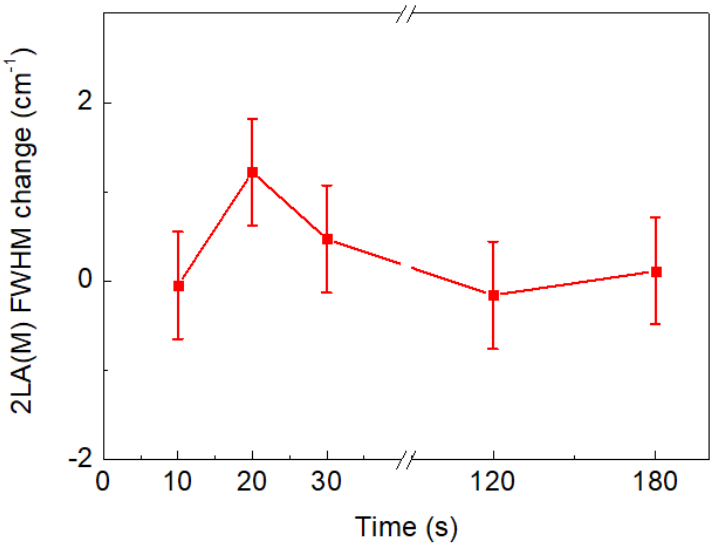

Figure 6.18: 2LA(M) mode FWHM variation as a function of treatment time (with fixed energy at 5 KeV).

Due to the its low signal-to-noise ratio, the low-wavenumber Raman spectra analysis employed in Part I was not applied here, since the peaks assignment would be not very precise in terms of the fitting parameters.

6.2.3 Atomic Force Microscopy

Figure 6.19 shows a representative micrograph of a pristine sample and the same sample after being subjected to a Helium beam of 500 eV for 10 s. It is possible to observe the treatment applied did not destroy or alter the morphology of triangular MoS_2 structures present. Once again, due to the growth process imperfections there are some non-monolayer structures present on the sample, and on the SiO_2 substrate.

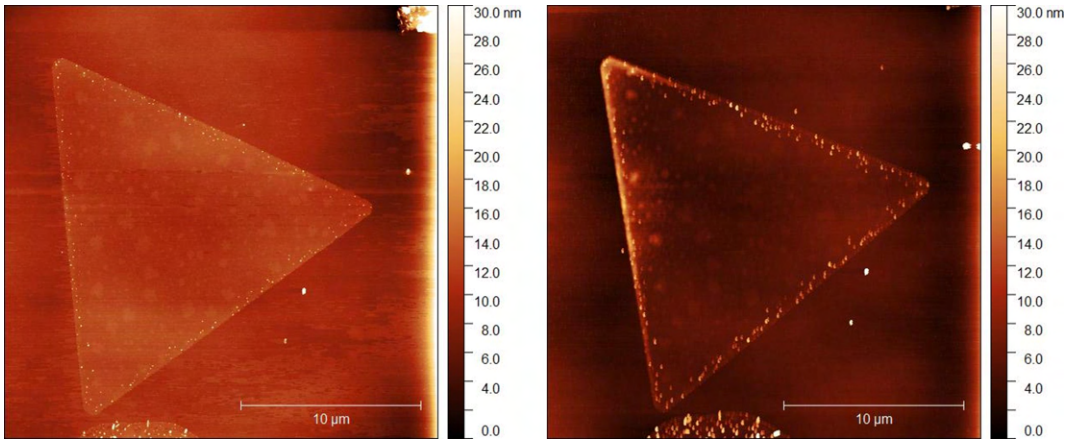

Figure 6.19: Representative micrograph of a pristine sample and the same sample after being subjected to a Helium beam of 500 eV for 10 s.

The MoS_2 step height was measured to confirm it was monolayer, as shown in figure 6.20. The measured height was 0.9 ± 0.2 nm in comparison to the SiO_2 flat surface. This value is comparable to other observations in literature [58, 59]. In this profile line an impurity at the border of the monolayer structure can be observed as its height differs slightly from the MoS_2 surface.

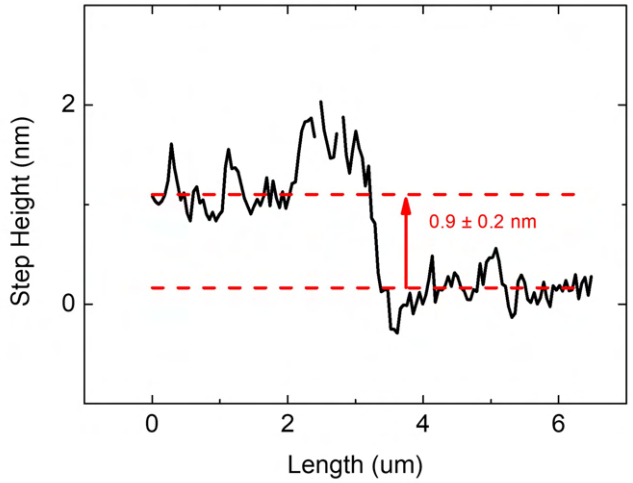

Figure 6.20: Profile showing the MoS_2 step height.

6.3 Discussion and Conclusions

In this second part of the thesis the initial goal of improving the monolayer MoS_2 was achieved using a Helium ion beam treatment. The CVD technique employed without salt proved to be more reliable regarding the reproducibility in comparison to the samples grown with NaBr salt in Part I. The PL spectra collected demonstrated an enhancement up two a factor of

2. The treatment time of 10 seconds using Helium ion beam energies of 50, 500, and 5000 eV were found to be the parameters that enhance the monolayer MoS_2 samples (table 6.3), while the other parameters tested resulted in a PL signal quenching. The treatments performed did not change the overall line shape of the PL emission, demonstrating the Helium ions did not induce a significant amount of defects in the MoS_2 crystal lattice. The deconvoluted exciton contributions showed the treatment induced the an increased amount of trions, meaning more defects such as Sulfur vacancies being created giving rise to the possibility of formation of such charged structures. The PL maps showed the achieved intensity increase is on the whole sample, not localized in a particular focused area. However, since the samples are manually positioned, if the sample is not correctly placed they can receive a different ion dose. This precise origin of the increased PL signal observed here is not clear and would need further investigation. It is possible it arises from the synergy of the different mechanisms described in chapter 3 within the crystal lattice, altering the band structure and exciton recombination. Another process that could be happening is a form of surface cleaning being promoted in the material, consequently increasing the measured emission (if this is true to some degree, the former is not excluded).

The resonant Raman analyses demonstrated that even the most intense treatment applied (5 KeV beam for 3 minutes) did not significantly change the spectral features besides the E′ mode quenching. The other treatments, specially the ones that resulted in increasing the PL signal intensity, induced very little change in comparison to the pristine spectrum. This controlled creation of defects also reflects in the 2LA(M) mode FWHM not increasing in the manner observed in the first part of the thesis. The AFM analysis revealed the structures morphology remain unchanged in the nanometer scale, this result was expected since during Part I no change was verified and in Part II the treatments applied were less intense.

7
Conclusion

The experiments conducted in this thesis aimed to enhance the photoluminescence (PL) emission of monolayer MoS_2 through different treatments on its surface, and this goal was ultimately achieved.

In the initial part, the Nitrogen plasma treatment did not reach the anticipated increase in PL emission. Despite this, valuable insights were gained. The AFM analysis confirmed the monolayer nature of the samples and their morphological integrity post-treatment. However, the CVD process requires refinement for practical device fabrication, especially concerning reproducibility and minimization of intermediate oxide debris. The PL analysis revealed a notable intensity quenching and increase in defects, evidenced by shifts in peak positions and the presence of trions becoming the main feature, suggesting Sulfur vacancies. Resonant Raman spectroscopy further corroborated these findings, indicating an evolution of spectroscopic features associated with defect density.

In contrast, the subsequent experiments employing Helium ion beam treatment achieved the desired enhancement in monolayer MoS_2. Utilizing the CVD technique without salt proved more reliable in terms of reproducibility. Significant improvements in PL emission, up to a factor of 2, were observed under specific treatment parameters (the best result was achieved using a 500 eV beam for 10 seconds), without inducing significant lattice defects. Deconvolution of exciton contributions revealed an increase in trions without becoming the main feature, indicating the creation of defects such as sulfur vacancies in a controllable manner. PL mapping confirmed the uniformity of the intensity increase across the sample, albeit caution is needed placing the samples for treatment. Resonant Raman analyses demonstrated minimal changes in spectral features, again reflecting controlled defect creation, the treatments in the second part exhibited limited impact in the 2LA(M) vibrational mode FWHM. AFM analysis confirmed the morphological integrity of the samples post-treatment, consistent with the expectation from less intense treatments.

Finally, while the Nitrogen plasma treatment did not achieve the initial goal, the Helium ion beam treatment proved successful in enhancing PL emission without compromising sample integrity. This enhancement via defect engineering was not previously reported in this range of time and energy parameters, and constitutes a fast method to improving this property in monolayer MoS_2.

7.1 Perspectives

Future research in the application of Helium ion treatments on MoS_2 should focus on refining treatment parameters and optimizing the experiments geometry for better scalability. This should also be extended to other TMDs such as WS_2. Fabrication techniques for practical applications outside laboratory context should also be improved. Another research perspective is the application in devices such as photodetectors and gas sensors, to check how much this PL enhancement improves the devices functionality. On a basic research perspective, other techniques could be employed to see the effect of the treatment in the structure (such as the crystal lattice), electronic properties, and chemical composition. This would further elucidate the process that enhances the photoluminescence emission.

8
Bibliography

[1] K. S. Novoselov, A. K. Geim, S. V. Morozov, D. Jiang, Y. Zhang, S. V. Dubonos, I. V. Grigorieva, and A. A. Firsov. Electric field effect in atomically thin carbon films. *Science*, 306(5696):666–669, 2004. Cited in page 16.

[2] Y. Kopelevich, S. Bud'ko, Daniel R. Cooper, Benjamin D'Anjou, Nageswara Ghattamaneni, Benjamin Harack, Michael Hilke, Alexandre Horth, Norberto Majlis, Mathieu Massicotte, Leron Vandsburger, Eric Whiteway, and Victor Yu. Experimental review of graphene. *ISRN Condensed Matter Physics*, 2012. Cited in page 16.

[3] Xuesong Li, Carl W. Magnuson, Archana Venugopal, Jinho An, Ji Won Suk, Boyang Han, Mark Borysiak, Weiwei Cai, Aruna Velamakanni, Yanwu Zhu, Lianfeng Fu, Eric M. Vogel, Edgar Voelkl, Luigi Colombo, and Rodney S. Ruoff. Graphene films with large domain size by a two-step chemical vapor deposition process. *Nano Letters*, 10(11):4328–4334, 2010. PMID: 20957985. Cited in page 16.

[4] Ke Cao, Shizhe Feng, Ying Han, Libo Gao, Thuc Hue Ly, Zhiping Xu, and Yang Lu. Elastic straining of free-standing monolayer graphene. *Nature Communications*, 2020. Cited in page 16.

[5] R. R. Nair, P. Blake, A. N. Grigorenko, K. S. Novoselov, T. J. Booth, T. Stauber, N. M. R. Peres, and A. K. Geim. Fine structure constant defines visual transparency of graphene. *Science*, 320(5881):1308–1308, 2008. Cited in page 16.

[6] Saju Joseph, Jainy Mohan, Seetha Lakshmy, Simil Thomas, Brahmananda Chakraborty, Sabu Thomas, and Nandakumar Kalarikkal. A review of the synthesis, properties, and applications of 2d transition metal dichalcogenides and their heterostructures. *Materials Chemistry and Physics*, 297:127332, 2023. Cited in page 16.

[7] Sajedeh Manzeli, Dmitry Ovchinnikov, Diego Pasquier, Oleg V. Yazyev, and Andras Kis. 2d transition metal dichalcogenides. *Nature Reviews Materials*, 2017. Cited 3 times in pages 10, 16, and 27.

[8] Jiadong Zhou, Junhao Lin, Xiangwei Huang, Yao Zhou, Yu Chen, Juan Xia, Hong Wang, Yu Xie, Huimei Yu, Jincheng Lei, Di Wu, Fucai Liu, Qundong Fu, Qingsheng Zeng, Chuang-Han Hsu, Changli Yang, Li Lu, Ting Yu, Zexiang

Shen, Hsin Lin, Boris I. Yakobson, Qian Liu, Kazu Suenaga, Guangtong Liu, and Zheng Liu. A library of atomically thin metal chalcogenides. *Nature*, 2018. Cited in page 16.

[9] Dung-Sheng Tsai, Keng-Ku Liu, Der-Hsien Lien, Meng-Lin Tsai, Chen-Fang Kang, Chin-An Lin, Lain-Jong Li, and Jr-Hau He. Few-layer mos2 with high broadband photogain and fast optical switching for use in harsh environments. *ACS Nano*, 7(5):3905–3911, 2013. PMID: 23590667. Cited in page 16.

[10] Nengjie Huo and Gerasimos Konstantatos. Recent progress and future prospects of 2d-based photodetectors. *Advanced Materials*, 30(51):1801164, 2018. Cited in page 16.

[11] Mingsheng Long, Peng Wang, Hehai Fang, and Weida Hu. Progress, challenges, and opportunities for 2d material based photodetectors. *Advanced Functional Materials*, 29(19):1803807, 2019. Cited in page 16.

[12] V. Podzorov, M. E. Gershenson, Ch. Kloc, R. Zeis, and E. Bucher. High-mobility field-effect transistors based on transition metal dichalcogenides. *Applied Physics Letters*, 84(17):3301–3303, 04 2004. Cited in page 16.

[13] Nengjie Huo, Sefaattin Tongay, Wenli Guo, Renxiong Li, Chao Fan, Fangyuan Lu, Juehan Yang, Bo Li, Yongtao Li, and Zhongming Wei. Novel optical and electrical transport properties in atomically thin wse2/mos2 p–n heterostructures. *Advanced Electronic Materials*, 1(5):1400066, 2015. Cited in page 16.

[14] Jhih-Wei Chen, Shun-Tsung Lo, Sheng-Chin Ho, Sheng-Shong Wong, Thi-Hai-Yen Vu, Xin-Quan Zhang, Yi-De Liu, Yu-You Chiou, Yu-Xun Chen, Jan-Chi Yang, Yi-Chun Chen, Ying-Hao Chu, Yi-Hsien Lee, Chung-Jen Chung, Tse-Ming Chen, Chia-Hao Chen, and Chung-Lin Wu. A gate-free monolayer wse2 pn diode. *Nature Communications*, 2018. Cited in page 16.

[15] Mingjun Yang, Haibo Shu, Yanyan Li, Dan Cao, and Xiaoshuang Chen. Polarization-induced band-alignment transition and nonvolatile p-n junctions in 2d van der waals heterostructures. *Advanced Electronic Materials*, 8(3):2101022, 2022. Cited in page 16.

[16] Qiyi Zhao, Yaohui Guo, Yixuan Zhou, Zehan Yao, Zhaoyu Ren, Jintao Bai, and Xinlong Xu. Band alignments and heterostructures of monolayer transition metal trichalcogenides mx3 (m = zr, hf; x = s, se) and dichalcogenides mx2 (m = tc, re; x=s, se) for solar applications. *Nanoscale*, 10:3547–3555, 2018. Cited in page 16.

[17] Dehui Deng, K. S. Novoselov, Qiang Fu, Nanfeng Zheng, Zhongqun Tian, and Xinhe Bao. Catalysis with two-dimensional materials and their heterostructures. *Nature Nanotechnology*, 2016. Cited in page 16.

[18] Yang Cao. Roadmap and direction toward high-performance mos2 hydrogen evolution catalysts. *ACS Nano*, 15(7):11014–11039, 2021. PMID: 34251805. Cited in page 16.

[19] Tianyi Zhang, Kazunori Fujisawa, Fu Zhang, Mingzu Liu, Michael C. Lucking, Rafael Nunes Gontijo, Yu Lei, He Liu, Kevin Crust, Tomotaroh Granzier-Nakajima, Humberto Terrones, Ana Laura Elías, and Mauricio Terrones. Universal in situ substitutional doping of transition metal dichalcogenides by liquid-phase precursor-assisted synthesis. *ACS Nano*, 14(4):4326–4335, 2020. PMID: 32208674. Cited in page 16.

[20] Yu Lei, Kazunori Fujisawa, Fu Zhang, Natalie Briggs, Amir Reza Aref, Yin-Ting Yeh, Zhong Lin, Joshua A. Robinson, Ramakrishnan Rajagopalan, and Mauricio Terrones. Synthesis of v-mos2 layered alloys as stable li-ion battery anodes. *ACS Applied Energy Materials*, 2(12):8625–8632, 2019. Cited in page 16.

[21] Yu Lei, Derrick Butler, Michael C. Lucking, Fu Zhang, Tunan Xia, Kazunori Fujisawa, Tomotaroh Granzier-Nakajima, Rodolfo Cruz-Silva, Morinobu Endo, Humberto Terrones, Mauricio Terrones, and Aida Ebrahimi. Single-atom doping of mos₂ with manganese enables ultrasensitive detection of dopamine: Experimental and computational approach. *Science Advances*, 6(32):eabc4250, 2020. Cited in page 16.

[22] Christian Schwermann, Torsten Stiehm, Philipp Tonndorf, Robert Schneider, Robert Schmidt, Johannes Kern, Steffen Michaelis de Vasconcellos, Rudolf Bratschitsch, and Nikos L. Doltsinis. Incorporation of oxygen atoms as a mechanism for photoluminescence enhancement of chemically treated mos2. *Phys. Chem. Chem. Phys.*, 20:16918–16923, 2018. Cited in page 16.

[23] Yichao Wang, Jian Zhen Ou, Sivacarendran Balendhran, Adam F. Chrimes, Majid Mortazavi, David D. Yao, Matthew R. Field, Kay Latham, Vipul Bansal, James R. Friend, Serge Zhuiykov, Nikhil V. Medhekar, Michael S. Strano, and Kourosh Kalantar-zadeh. Electrochemical control of photoluminescence in two-dimensional mos2 nanoflakes. *ACS Nano*, 7(11):10083–10093, 2013. PMID: 24148149. Cited in page 16.

[24] Yu Zhang, Yuyu Yao, Marshet Getaye Sendeku, Lei Yin, Xueying Zhan, Feng Wang, Zhenxing Wang, and Jun He. Recent progress in cvd growth of

2d transition metal dichalcogenides and related heterostructures. *Advanced Materials*, 31(41):1901694, 2019. Cited in page 18.

[25] Luzhao Sun, Guowenand Yuan, Liboand Gao, Jieunand Yang, Manishand Gharahcheshmeh Chhowalla, Meysam Heydari, Karen K. Gleason, Yong Seok Choi, Byung Hee Hong, and Zhongfan Liu. Chemical vapour deposition. *Nature Reviews Methods Primers*, 2021. Cited 2 times in pages 10 and 19.

[26] Ado Jorio, Mildred S. Dresselhaus, Riichiro Saito, and Gene Dresselhaus. *Raman Spectroscopy in Graphene Related Systems*, chapter 4. John Wiley & Sons, Ltd, 2011. Cited 3 times in pages 10, 20, and 22.

[27] C. V. RAMAN and K. S. KRISHNAN. A new type of secondary radiation. *Nature*, 1928. Cited in page 20.

[28] R Saito, Y Tatsumi, S Huang, X Ling, and M S Dresselhaus. Raman spectroscopy of transition metal dichalcogenides. *Journal of Physics: Condensed Matter*, 28(35):353002, jul 2016. Cited in page 22.

[29] Carlos F. G. C. Geraldes. Introduction to infrared and raman-based biomedical molecular imaging and comparison with other modalities. *Molecules*, 25(23), 2020. Cited 2 times in pages 10 and 23.

[30] J.R. Lakowicz. *Principles of Fluorescence Spectroscopy*. Springer, 2006. Cited in page 23.

[31] Takeshi Aoki. *Photoluminescence Spectroscopy*, pages 1–12. John Wiley & Sons, Ltd, 2012. Cited in page 23.

[32] Hiba Alhalaby, Haitham Zaraket, and Maria Principe. Enhanced photoluminescence with dielectric nanostructures: A review. *Results in Optics*, 3:100073, 2021. Cited 2 times in pages 10 and 24.

[33] G. Binnig, C. F. Quate, and Ch. Gerber. Atomic force microscope. *Phys. Rev. Lett.*, 56:930–933, Mar 1986. Cited in page 24.

[34] Ernst Meyer; Roland Bennewitz; Hans J. Hug. *Scanning Probe Microscopy: The Lab on a Tip*. Springer Nature, 2021. Cited 2 times in pages 10 and 25.

[35] Xiao Li and Hongwei Zhu. Two-dimensional mos2: Properties, preparation, and applications. *Journal of Materiomics*, 1(1):33–44, 2015. Cited in page 26.

[36] Hui Chen, Jiwei Zhang, Dongxiao Kan, Jiabei He, Mengshan Song, Jianhua Pang, Songrui Wei, and Kaiyun Chen. The recent progress of two-dimensional transition metal dichalcogenides and their phase transition. *Crystals*, 12(10), 2022. Cited 2 times in pages 10 and 26.

[37] K. S. Novoselov, D. Jiang, F. Schedin, T. J. Booth, V. V. Khotkevich, S. V. Morozov, , and A. K. Geim. Two-dimensional atomic crystals. *Proceedings of the National Academy of Sciences*, 2005. Cited in page 27.

[38] Andrea Splendiani, Liang Sun, Yuanbo Zhang, Tianshu Li, Jonghwan Kim, Chi-Yung Chim, Giulia Galli, and Feng Wang. Emerging photoluminescence in monolayer mos2. *Nano Letters*, 10(4):1271–1275, 2010. PMID: 20229981. Cited 3 times in pages 10, 27, and 28.

[39] Heather M. Hill, Albert F. Rigosi, Kwang Taeg Rim, George W. Flynn, and Tony F. Heinz. Band alignment in mos2/ws2 transition metal dichalcogenide heterostructures probed by scanning tunneling microscopy and spectroscopy. *Nano Letters*, 16(8):4831–4837, 2016. PMID: 27298270. Cited in page 27.

[40] Hong Li, Qing Zhang, Chin Chong Ray Yap, Beng Kang Tay, Teo Hang Tong Edwin, Aurelien Olivier, and Dominique Baillargeat. From bulk to monolayer mos2: Evolution of raman scattering. *Advanced Functional Materials*, 22(7):1385–1390, 2012. Cited 2 times in pages 10 and 28.

[41] Xiaodong Xu, Wang Yao, Di Xiao, and Tony F. Heinz. Spin and pseudospins in layered transition metal dichalcogenides. *Nature Physics*, 2014. Cited in page 28.

[42] Jason W. Christopher, Bennett B. Goldberg, and Anna K. Swan. Long tailed trions in monolayer mos2: Temperature dependent asymmetry and resulting red-shift of trion photoluminescence spectra. *Scientific Reports*, 2017. Cited 3 times in pages 10, 28, and 29.

[43] Narae Kang, Hari P. Paudel, Michael N. Leuenberger, Laurene Tetard, and Saiful I. Khondaker. Photoluminescence quenching in single-layer mos2 via oxygen plasma treatment. *The Journal of Physical Chemistry C*, 118(36):21258–21263, 2014. Cited 2 times in pages 30 and 43.

[44] Suhhyun Kim, Min Sup Choi, Deshun Qu, Chang Ho Ra, Xiaochi Liu, Minwoo Kim, Young Jae Song, and Won Jong Yoo. Effects of plasma treatment on surface properties of ultrathin layered mos2. *2D Materials*, 3(3):035002, jul 2016. Cited in page 30.

[45] Anh Duc Nguyen, Tri Khoa Nguyen, Chinh Tam Le, Sungdo Kim, Farman Ullah, Yangjin Lee, Sol Lee, Kwanpyo Kim, Dooyong Lee, Sungkyun Park, Jong-Seong Bae, Joon I. Jang, and Yong Soo Kim. Nitrogen-plasma-treated continuous monolayer mos2 for improving hydrogen evolution reaction. *ACS Omega*, 4(25):21509–21515, 2019. PMID: 31867547. Cited 4 times in pages 10, 31, 32, and 65.

[46] Angelica Azcatl, Xiaoye Qin, Abhijith Prakash, Chenxi Zhang, Lanxia Cheng, Qingxiao Wang, Ning Lu, Moon J. Kim, Jiyoung Kim, Kyeongjae Cho, Rafik Addou, Christopher L. Hinkle, Joerg Appenzeller, and Robert M. Wallace. Covalent nitrogen doping and compressive strain in mos2 by remote n2 plasma exposure. *Nano Letters*, 16(9):5437–5443, 2016. PMID: 27494551. Cited in page 31.

[47] Muhammad Waqas Iqbal, Kinza Shahzad, Rehan Akbar, and Ghulam Hussain. A review on raman finger prints of doping and strain effect in tmdcs. *Microelectronic Engineering*, 219:111152, 2020. Cited 2 times in pages 31 and 44.

[48] Jue Wang, Xichen Feng, Daniel Hedman, Xiaohua Wu, Haiyang Pan, and Qinfang Zhang. Enhancing the hydrogen evolution reaction on mos2 flakes by cold plasma treatment. *Electrochemistry Communications*, 137:107250, 2022. Cited 2 times in pages 32 and 65.

[49] André do Nascimento Barbosa, Cesar Augusto Diaz Mendoza, Neileth Johanna Stand Figueroa, Mauricio Terrones, and Fernando Lázaro Freire Júnior. Luminescence enhancement and raman characterization of defects in ws2 monolayers treated with low-power n2 plasma. *Applied Surface Science*, 535:147685, 2021. Cited 2 times in pages 32 and 43.

[50] Jakub Jadwiszczak, Gen Li, Conor P. Cullen, Jing Jing Wang, Pierce Maguire, Georg S. Duesberg, James G. Lunney, and Hongzhou Zhang. Photoresponsivity enhancement in monolayer MoS2 by rapid O2:Ar plasma treatment. *Applied Physics Letters*, 114(9):091103, 03 2019. Cited in page 32.

[51] Jitao Li, Jing Bai, Ming Meng, Chunhong Hu, Honglei Yuan, Yan Zhang, and Lingling Sun. Improved temporal response of mos2 photodetectors by mild oxygen plasma treatment. *Nanomaterials*, 12(8), 2022. Cited in page 33.

[52] Binjie Huang, Feng Tian, Youde Shen, Minrui Zheng, Yunshan Zhao, Jing Wu, Yi Liu, Stephen J. Pennycook, and John T. L. Thong. Selective engineering of chalcogen defects in mos2 by low-energy helium plasma. *ACS Applied*

Materials & Interfaces, 11(27):24404–24411, 2019. PMID: 31199625. Cited 4 times in pages 10, 33, 34, and 57.

[53] Shayani Parida, Yongqiang Wang, Huan Zhao, Han Htoon, Theresa Marie Kucinski, Mikhail Chubarov, Tanushree Choudhury, Joan Marie Redwing, Avinash Dongare, and Michael Thompson Pettes. Tuning of the electronic and vibrational properties of epitaxial mos2 through he-ion beam modification. *Nanotechnology*, 34(8):085702, dec 2022. Cited 4 times in pages 10, 34, 35, and 58.

[54] Rodrigo Gomes Costa, André do Nascimento Barbosa, Marcelo Eduardo Huguenin Maia da Costa, and Fernando Lázaro Freire. Resonance raman spectroscopy of mos2 monolayers treated with nitrogen plasma. *Vibrational Spectroscopy*, 123:103454, 2022. Cited 2 times in pages 37 and 65.

[55] Syed Hamza Safeer, Marcus V. O. Moutinho, Arthur R. J. Barreto, Braulio Soares Archanjo, Omar Ginoble Pandoli, Marco Cremona, Marcelo Eduardo Huguenin Maia da Costa, Fernando Lazaro Freire, and Victor Carozo. Sodium-mediated low-temperature synthesis of monolayers of molybdenum disulfide for nanoscale optoelectronic devices. *ACS Applied Nano Materials*, 4(4):4172–4180, 2021. Cited in page 37.

[56] David Nečas and Petr Klapetek. Gwyddion: an open-source software for spm data analysis. *Open Physics*, 10(1):181–188, 2012. Cited in page 39.

[57] Jiashuo Yan, Shuang Lian, Zhigang Cao, Yadan Du, Ping Wu, Huijuan Sun, and Yukai An. Cvd controlled preparation and growth mechanism of 2h-ws2 nanosheets. *Vacuum*, 207:111564, 2023. Cited in page 41.

[58] Fei Chen, Qiuran Lv, Yuan Xia, Shuduan Mao, and Yajie Li. Controllable synthesis of large-scale monolayer mos2 dendritic flakes with serrated edges and their multimodal microscopy and afm characterizations. *The Journal of Physical Chemistry C*, 126(31):13449–13457, 2022. Cited 2 times in pages 42 and 68.

[59] Ki Hoon Shin, Min-Kyu Seo, Sangyeon Pak, A-Rang Jang, and Jung Inn Sohn. Observation of strong interlayer couplings in ws2/mos2 heterostructures via low-frequency raman spectroscopy. *Nanomaterials*, 12(9), 2022. Cited 2 times in pages 42 and 68.

[60] Haiyan Nan, Zilu Wang, Wenhui Wang, Zheng Liang, Yan Lu, Qian Chen, Daowei He, Pingheng Tan, Feng Miao, Xinran Wang, Jinlan Wang, and Zhenhua Ni. Strong photoluminescence enhancement of mos2 through defect

engineering and oxygen bonding. *ACS Nano*, 8(6):5738–5745, 2014. PMID: 24836121. Cited 2 times in pages 43 and 47.

[61] Maria O'Brien, Nils Scheuschner, Janina Maultzsch, Georg S. Duesberg, and Niall McEvoy. Raman spectroscopy of suspended mos2. *physica status solidi (b)*, 254(11):1700218, 2017. Cited in page 44.

[62] Kapildeb Dolui, Ivan Rungger, Chaitanya Das Pemmaraju, and Stefano Sanvito. Possible doping strategies for mos_2 monolayers: An ab initio study. *Phys. Rev. B*, 88:075420, Aug 2013. Cited in page 44.

[63] Qu Yue, Shengli Chang, Shiqiao Qin, and Jingbo Li. Functionalization of monolayer mos2 by substitutional doping: A first-principles study. *Physics Letters A*, 377(19):1362–1367, 2013. Cited in page 44.

[64] Bruno R. Carvalho, Yuanxi Wang, Sandro Mignuzzi, Debdulal Roy, Mauricio Terrones, Cristiano Fantini, Vincent H. Crespi, Leandro M. Malard, and Marcos A. Pimenta. Intervalley scattering by acoustic phonons in two-dimensional mos2 revealed by double-resonance raman spectroscopy. *Nature Communications*, 2017. Cited 2 times in pages 45 and 47.

[65] J.M. Chen and C.S. Wang. Second order raman spectrum of mos2. *Solid State Communications*, 14(9):857–860, 1974. Cited in page 46.

[66] Tsachi Livneh and Jonathan E Spanier. A comprehensive multiphonon spectral analysis in mos2. *2D Materials*, 2(3):035003, jun 2015. Cited in page 46.

[67] Rafael N. Gontijo, Geovani C. Resende, Cristiano Fantini, and Bruno R. Carvalho. Double resonance raman scattering process in 2d materials. *Journal of Materials Research*, 2019. Cited in page 46.

[68] Sandro Mignuzzi, Andrew J. Pollard, Nicola Bonini, Barry Brennan, Ian S. Gilmore, Marcos A. Pimenta, David Richards, and Debdulal Roy. Effect of disorder on raman scattering of single-layer mos_2. *Phys. Rev. B*, 91:195411, May 2015. Cited in page 46.

[69] Jiake Li, Weitao Su, Fei Chen, Li Fu, Su Ding, Kaixin Song, Xiwei Huang, and Lijie Zhang. Atypical defect-mediated photoluminescence and resonance raman spectroscopy of monolayer ws2. *The Journal of Physical Chemistry C*, 123(6):3900–3907, 2019. Cited in page 48.

[70] Kazunori Fujisawa, Bruno R. Carvalho, Tianyi Zhang, Néstor Perea-López, Zhong Lin, Victor Carozo, Sérgio L. L. M. Ramos, Ethan Kahn, Adam Bolotsky, He Liu, Ana Laura Elías, and Mauricio Terrones. Quantification

and healing of defects in atomically thin molybdenum disulfide: Beyond the controlled creation of atomic defects. *ACS Nano*, 15(6):9658–9669, 2021. PMID: 33754710. Cited in page 49.

[71] Bureau international Des poids et mesures. *Le Système international d'unités (SI)*. BIPM, 2022. Cited in page 53.